Heliyon 9 (2023) e16583

Contents lists available at ScienceDirect

Heliyon

journal homepage: www.cell.com/heliyon

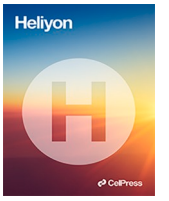

Research article

# Powder plasma spheroidization treatment and the characterization of microstructure and mechanical properties of SS 316L powder and L-PBF builds

E. Getto [a,*], R.J. Santucci Jr. [a,b,**], J. Gibbs [a], R. Link [a], E. Retzlaff [a], B. Baker [a], M. Koul [a], B. Croom [c], T. Montalbano [c], S. Storck [c], E. Cimpoiasu [a], E. Farnan [a]

[a] United States Naval Academy, 590 Holloway Rd, Annapolis, MD, 21042, USA
[b] U.S. Naval Research Laboratory, 4555 Overlook Rd, Washington, D.C, 20375, USA
[c] Johns Hopkins University Applied Physics Laboratory, 11100 Johns Hopkins Rd, Laurel, MD, 20723, USA

ARTICLE INFO

*Keywords:*
Stainless steel 316L
Laser powder bed fusion
Plasma spheroidization
Selective laser melting
Powder morphology

ABSTRACT

A plasma spheroidization treatment was applied to stock stainless steel 316L powder for additive manufacturing. The normal and treated powders were compared both in the powder state as well as in the resulting laser powder bed fusion (L-PBF) builds. The plasma spheroidization process slightly increased treated powder aspect ratio and sphericity and shifted the size distribution to larger diameters relative to the normal powder. The normal powder was austenitic in nature whereas the plasma spheroidization process introduced a small fraction (~3.5 vol %) of ferrite in the treated powder. Ferrite in the powder was not retained in the printed samples and was not shown to negatively affect the build quality. Porosity areal fraction was generally smaller in the treated powder builds. The normal powder builds had a 6% higher yield strength than treated, however the scatter was significantly larger in the 45° and horizontal orientations compared to the treated powder builds.

## 1. Introduction

Additive manufacturing (AM) technologies (also known as 3-D printing) offer several advantages over conventional manufacturing processes which have previously been used in the medical, energy, aerospace, defense, and other industries [1]. This includes the ability to incrementally direct a build process layer by layer, yielding final parts that are built to near net shape such that little or no additional machining is required after printing [2]. Further, the additive process permits the fabrication of geometries that are unachievable via traditional subtractive manufacturing as fabrication in layers permits printing internal features such as lattice structure or cooling channels [3].

Laser powder bed fusion (L-PBF), also known as selective laser melting (SLM), proceeds sequentially in a series of steps that repeat with each layer. A representative schematic of the scanning of a single layer is shown in Fig. 1. Initially, a thin layer of powder of the final alloy is spread over the build plate (first layer). After recoating is complete, the energy source-a laser in the case of L-PBF- is selectively scanned over the powder layer to fully melt and fuse the new layer to the previous part layers and/or support structure. The

* Corresponding author. 590 Holloway Rd, Annapolis, MD, 21042, USA.
** Corresponding author. U.S. Naval Research Laboratory, 4555 Overlook Rd, Washington, D.C. 20375, USA.
*E-mail addresses:* getto@usna.edu (E. Getto), raymond.santucci@nrl.navy.mil (R.J. Santucci).

https://doi.org/10.1016/j.heliyon.2023.e16583
Received 10 May 2023; Received in revised form 19 May 2023; Accepted 22 May 2023
Available online 24 May 2023

build plate is then recessed by the desired fused layer height and the next powder layer is spread. A quality build requires a consistently repeatable powder layer application process which is, itself, predicated on the powder spreadability and size distribution. A further challenge arising from the L-PBF methods noted by Glicksman et al. is that owing to the extremely high thermal gradients and attendant rapid solidification front velocities present, as-printed microstructure in L-PBF is highly anisotropic with the preferential development of columnar grains oriented in the build (Z) direction [4]. A number of other defects have been observed to limit L-PBF part quality including inclusion of voids in the build due to denudation of the powder layer [5], underfusion of powder and micro-cracking [6], deposition of spatter and metal vapor condensate noted by Ref. [7], and finally high energy density keyholing observed [8].

Several investigations have assessed the role powder metallurgy plays in the additive manufacturing process. A review by Sutton et al. asserted that powder feedstock can be characterized in terms of particle alloy composition, morphology, and microstructure [9]. The chemical composition of the powder will obviously affect the composition of the final build. Additionally, the chemical purity of the feedstock influences the melting and solidification of the melt pool, and the presence of impurities or contamination of the powder may promote undesirable alloy microstructure such as intermetallic phases. Any high temperature process is subject to changing material composition, primarily by facilitating oxidation reactions or volatilization of select elements. For instance, Zhou et al. printed a novel Ti alloy using selective laser melting and then observed surface oxidation of powder which was linked to increased build porosity [10], which can result naturally over time or when the powder is elevated in temperature, such as during powder manufacturing of AIS SS 316L [11] or, observed in Ti–6Al–4V when powder recycling from build-to-build is utilized [12]. Likewise, a powder may have a different composition from the raw material from which it was made depending upon the manufacturing parameters. The build process itself may result in compositional changes from the powder if volatilization is significant.

Powder morphology encompasses powder size, size distribution, and shape and is perhaps the most important particle characteristic in determining build quality [9]. Liu et al. observed that a tight size distribution yielded higher ultimate tensile strength and hardness in the SLM builds, while wide distributions yielded more dense parts with lower surface roughness [13]. The printing parameters, particularly the cons, z, are selected for the given powder size distribution. Bierwagen and Sanders observed that excessively large particles tended to reduce powder packing density compared to smaller, space-filling particles [14]. However, Simchi also noted issues with excessively small particles which have the propensity to agglomerate and skid over the powder bed during recoating [15]. Overall, powder shape also influences flowability and packing. Powder shape also influences flowability and packing. Spherical particles have a higher packing efficiency and spread more homogenously compared to irregularly shaped particles [16]. Smoother particles are also desirable as they contain fewer points of contact to contribute to particle-to-particle friction, resulting in better spreading to allow proper in-filling during recoating for both SLM and electron beam melting (EBM) prints [17]. Finally, the local packing density and uniformity of the powder layer thickness heavily influences the laser-powder interaction, as the cavities between and among powder particles dramatically increases overall energy absorption [18].

Powder microstructure is also important to consider in the AM process, as the microstructure of the powder influences that of the build. For example, stainless steels, as a class of materials, contain a mix of austenite, ferrite, or martensite phases, even within a specific alloy designation. For instance, Starr et al. observed that 17–4 PH steel powder can be gas atomized in a nitrogen environment to yield an austenitic structure, while a martensitic structure can be prepared in an argon environment [19]. The martensitic powder bore a martensitic build regardless of the build environment, whereas the austenitic powder retained more austenite in the build microstructure for a nitrogen atmosphere than an argon atmosphere. Similarly, γ-austenitic 316 stainless steel powder can accumulate δ-ferrite phase as it is continually reused from build cycle to build cycle as observed by both Heiden et al. [20] and Pinto et al. [21], which could be potentially disadvantageous to the build quality due to irregularities from magnetism-induced clustering of the ferrite-containing particles, as hypothesized by the authors. Concerns with powder quality motivates research into powder treatment processes that optimize powder properties for AM technologies.

The powder processing technique examined in this study utilizes thermal plasma technology developed by Taylor and Pirzada [22]. An inert gas is ionized using an inductively coupled plasma torch which produces extremely high temperatures (2000–20,000 K) localized to the confinement region of the plasma within the inductive coil illustrated by (Fig. 2, components 3 and 4) [23]. Argon is

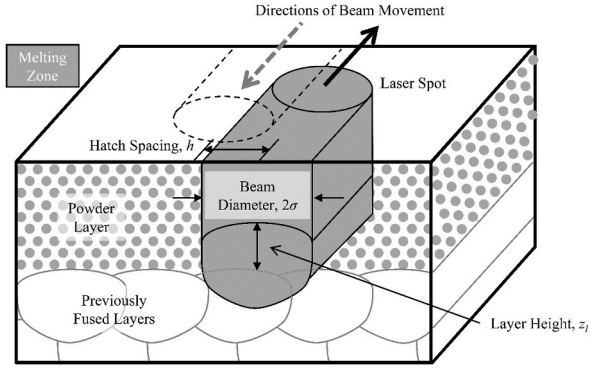


**Fig. 1.** Basic geometry relevant for normalization of L-PBF process parameters.

used as a plasma gas as its monotonic nature requires lower power to ionize. The addition of diatomic plasma gases will determine the processing chemistry for the desired application (reductive or oxidative) and results in a plasma of higher energy and thermal conductivity. The plasma powder processing technique being described in this study is often called spheroidization. Non-spherical precursor particles (fibrils, flakes or plate-like) are fed into a carrier gas and move through the very high temperatures in the plasma confinement chamber, melting very quickly while in flight. To minimize the surface energy, the liquid particles take a spherical shape. Upon exiting the plasma, the spheroidized particles are quenched and solidify in the steep temperature gradient and are collected at the bottom of the plasma chamber (Fig. 2). A number of ceramic oxides, metals and alloy precursors are successfully spheroidized on a commercial scale using this technology [22].

The stainless steel 316L (SS 316L) powders used in this study were initially produced using gas atomization and enter the plasma process as fairly spherical. Ji et al. claimed that plasma processing of gas atomized particles can further refine the powder size distribution, which can improve flowability and packing [24]. The plasma process eliminates internal cavities and fractures in the precursor particles and improves densification. It also smooths the particle surfaces, reducing contamination during transport. This process also enhances the powder purity through the reactive vaporization of impurities and has applications for extending the life of recycled powders by eliminating contaminates like oxygen [25]. All these factors serve to potentially improve the quality of an AM part. Studies in SS 316L specifically have shown that the plasma process reduces both the carbon and sulfur content and increases the silicon content in gas atomized powder. Studies in SS 316L specifically have shown that the plasma process reduces both the carbon and sulfur content and increases the silicon content in gas atomized powder. It also introduces delta ferrite due to the rapid cooling that occurs [24].

Therefore, the objective of this paper is to assess the powder spheroidization treatment of feedstock powder and its effect on the microstructure and mechanical properties of L-PBF SS 316L. This will be accomplished by assessing the microstructure and macrostructure of the powder, the microstructure of the built parts and the mechanical properties of the resulting build. The specific effects of delta ferrite and powder morphology on the resulting porosity and mechanical properties of the build will be highlighted. All other variables will be held constant so the specific effect of the powder treatment can be addressed.

## 2. Material and methods

### 2.1. Powder spheroidization

Fig. 2 shows the powder spheroidization process. Gas atomized SS 316L powder was processed using a 15 kW Tekna RF Plasma System. Powder was introduced to the plasma treatment by a Tekna PFD series disc feeder system stabilized at 25–30 g/min which has been shown to result in a spheroidization rate of nearly 100%. The inductively coupled plasma torch was powered by an RF power source to generate high temperature and high enthalpy conditions in the chamber as described in the Introduction. The plasma treatment and collection process were performed under argon gas with a torch sheath gas comprised of a mixture of 3.6% hydrogen and 96.4% argon. Powder was allowed to cool under argon gas and periodic collections from the chamber base were performed hourly. Collected powder was sieved using a #270 mesh vibratory system to remove agglomerated particles and/or melt scrap. Going forward, the as received powder will be referred to as “normal” and the processed powder will be referred to as “treated.”

### 2.2. Powder characterization

The elemental composition of the powder and build samples was characterized with X-ray fluorescence (XRF). Samples were loaded in a low-vacuum chamber and probed with a 30 keV Rh X-ray source. Each sample was assessed for 2 min for each location with five different locations tested per sample.

A Camsizer X2® was used to measure the particle size, distribution, and shape characteristics. The Camsizer X2® uses two high-speed optical cameras to measure the particles. The particles are measured in a dry dispersion by compressed air at a pressure of 20 kPa. A velocity profile of the particles was created and applied to the measurements to ensure that the same particles are not measured twice. The particle size is determined from the smallest of all maximum chords of the particle projection ($X_{c\ min}$). The values reported for the D (10), D (50), and D (90),[1] as well as the shape characteristics, are the result of averaging three trials. The average sample size was 1,270,000 particles for the normal powder and 924,000 particles for the treated powder, per trial. All reported measurements are on a volume basis.

Bulk crystal phase analysis was assessed by X-ray diffraction utilizing an X’Pert Pro Panalytical diffractometer. Powder and built samples were analyzed in a spinning stage with a rotational speed of 1 revolution per second. Powder was packed and levelled in the sample stage. Thin discs were sectioned from the bottom, middle, and top of the SLM printed bars and mounted and levelled in the sample stage with putty. The X-ray probe was generated from a copper anode at an accelerating voltage of 45 keV and a 40 mA current. The diffraction pattern was surveyed from a 2θ of 20°–100° at 2θ increments of 0.00657°.

Powder and builds were also analyzed in a scanning electron microscope (SEM) with secondary electron detector (SE), electron backscatter diffraction (EBSD), and energy dispersive X-ray spectroscopy (EDS). Powder was also mounted in a conductive epoxy resin prior to polishing with a standard suite of grinding papers up to #1200 grit followed by diamond polishing up to 3 μm and a final

[1] D(10) means that 10% of the particles were less than the reported diameter.

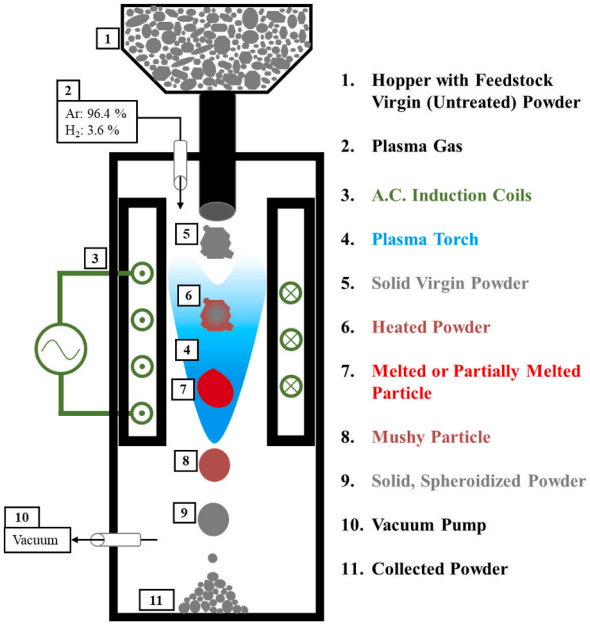


**Fig. 2.** Thermal plasma technology used in "spheroidizing" processing of SS 316L powder.

vibratory polishing in 0.5 μm colloidal silica solution for at least 4 h prior to EBSD. All analysis was conducted on a Tescan Mira SEM operating at 20 kV with 8.4 nA beam current.

EBSD and EDS scans were collected utilizing the Texture and Elemental Analytical (TEAM) software from EDAX and grain diameter misorientation angle were analyzed using Orientation Imaging Microscopy (OIM) Analysis v7, also from EDAX. Prior to analysis, scans were "cleaned" using the neighbor confidence interval (CI) correlation and grain CI standardization algorithms. All microstructure analysis (grain diameter, grain mean average misorientation angle) was performed in the OIM software or FIJI software [26].

A Quantum Design vibrating sample magnetometer (VSM) was utilized to assess the magnetic characteristics of each powder sample at 300 K. The magnetic moment of the powder sample (~0.1 g) was measured as the magnetic field was applied in a forward sweep to 40 kOe, then in a reverse sweep to −40 kOe, and again in a forward sweep to 40 kOe. The sample oscillated at a frequency of 40 Hz and an amplitude of 2 mm. Supporting data is provided in an open access data repository [27].

### 2.3. L-PBF printing of samples

All samples used for analysis were fabricated using a GE Concept Laser Cusing Mlab R printer with builds prepared on 90 mm × 90 mm, SS 316L build plates with approximately 6 mm of support structure for each sample. The builds with the normal powder were fabricated and the machine underwent a thorough cleaning prior to the introduction of the treated powder stock. Powder was loaded into the powder well of the machine and compacted manually using a plate compaction tool as recommended by GE Concept Laser. The Mlab featured a YLM-100-AC Ytterbium laser with 100 W capacity in continuous wave mode with wavelength of 1070 nm. The machine also featured a compliant recoater blade which was replaced between builds. Individual builds were arranged in each of three fabrication directions: X, XZ, and Z. In this study, X is a direction that lies within the plane of the build plate and will be referred to as "*horizontal*", XZ will be referred to as "*45°*" and Z, the direction perpendicular to the build plate, will be referred to as "*vertical.*" These notional orientations are shown relative the build plate, recoating direction and build direction in Fig. 3. The X and Y direction were treated indiscriminately. A total of 8 builds were completed, 4 using the normal SS 316L powder and 4 using the treated powder. Due to the space limitations of the build volume, a suitable number of horizontal sample bars required two separate prints for each powder type. The builds were printed under inert nitrogen conditions using the "cl 20_performanceCusing_100_V2" parameter set provided by Concept Laser, with the specific printing parameters listed in Table 1. The build plate was not heated. Of note, an island laser scanning strategy was used featuring 10 mm × 10 mm rasters that translated 2 mm in the x and y directions between layers with infill orientation also rotating 67° between layers. Hann et al. [28] proposed assessing the energy density of an SLM process using the dimensionless normalized enthalpy parameter, $\Delta H/h_s = AP/[\rho h_s (\pi D v \sigma^3)^{0.5}]$. Using a thermal diffusivity, D, for 316L of $1.01\times10^{-5}$ W/m$^2$, a density of 7.98 kg/m$^3$, and a total enthalpy at the melt point, $h_s$, of $1.2 \times 10^3$ kJ/kg [18]; the processing parameters of Table 1 yield a normalized enthalpy value, $\Delta H/h_s$, of 6.89 when a laser absorptivity, $A$, of 0.4 is assumed [29]. This is well below the experimental keyhole threshold of approximately 33 observed by King et al. [18] and is expected to produce conduction mode melt tracks. The tensile test samples were printed as cylindrical blanks of diameter 7.62 mm and length of 57 mm and were later machined to a 4.06 mm gage section.

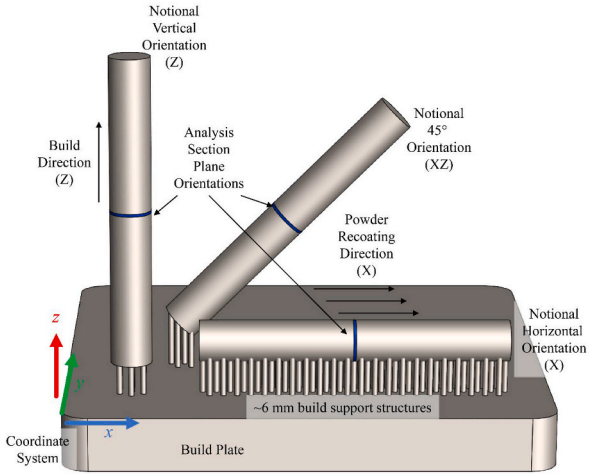


**Fig. 3.** Notional build orientation and build support structures of the tensile test sample blanks with respect to the build plate and build and recoating directions. Horizontal and 45° orientation samples incorporated additional rotation about the z-axis (not shown) to support efficient build processing and recoating (avoiding impacting the compliant recoater blade with multiple leading edges of the build at the same time). Analysis section slices are shown in blue and are perpendicular to the long axis of the build orientation. (For interpretation of the references to colour in this figure legend, the reader is referred to the Web version of this article.)

**Table 1**
Mlab R processing parameters for the "cl 20_performanceCusing_100_V2" printer setting, as reported by GE Concept Laser. Build plates are held at ambient temperature.

| $P$, Laser Power (W) | 90 |
|---|---|
| $v$, Scan Speed (mm/s) | 600 |
| $\sigma$, Beam Half Diameter ($\mu$m) | 25 |
| $h$, Hatch Spacing (infill) ($\mu$m) | 84 |
| $z_l$, Layer Height ($\mu$m)[a] | 25 |
| $\Delta H/h_s$, Normalized Enthalpy (−) [28] | 6.89 |
| Island Infill Dimensions (mm) | 10 × 10 |
| Inter-layer Scan Rotation Angle | 67° |
| Inter-layer Island Indexing (mm) | 2 (both x and y) |

[a] Layer height refers specifically to the step size for the build platform. Due to consolidation of the powder bed into the fused layer, the powder overburden depth, in layers well above the base plate, is typically 3.3 times as tall [30].

### 2.4. Build characterization

SEM of the build was performed with the same polishing and imaging parameters as for the powder. Additionally, pore areas were measured in FIJI software with each pore area calculated using the polygon tool. Three micrographs per sample of ~2000 μm × ~2000 μm were assessed. The mean equivalent sphere diameter was calculated according to Equation (1):

$$d_{eq} = 2\left(\frac{A}{\pi}\right)^{1/2} \quad (1)$$

The porosity was assessed by calculating the porosity area fraction from the total area of pores divided by the micrograph areas (Equation (2)). Error bars were taken from the resolution of the instrument and taken as 2 pixels (~1 nm) and propagated through the diameter and porosity calculations.

$$\frac{\Delta A}{A} = \frac{\sum_{i=1}^{n} A_{pore}}{\sum_{i=1}^{3} A_{image}} \quad (2)$$

Cylinders of the as-printed SS 316L samples were imaged using X-ray Computed Tomography (XCT) to resolve the internal porosity. Imaging was performed using a NorthStar Imaging X-50 system, equipped with a FeinFocus FXE 225 keV X-ray source and a Varian L07 imaging panel. The sample was imaged at 20 μm voxel size, with 1801 projections, and X-ray source settings of 200 keV and 90 μA. The

total scan time was 20 min per sample. The scans were reconstructed using a standard filtered backprojection algorithm. The reconstructed volumes were processed using Volume Graphics (VGStudio Max 3.4) to measure the internal porosity. The porosity was extracted using the EasyPore thresholding algorithm, which was tuned to ignore XCT reconstruction artifacts as well as pores smaller than 8 voxels in size.

### 2.5. Tensile behavior and fractography

Tensile tests were performed on samples oriented in the *horizontal* (X), *vertical* (Z), and *45°* (XZ) orientation per ASTM F2971-13 [31]. Either 9 or 10 replicate tests were performed for each powder and each orientation using 4.06 mm dia. Round tensile specimens machined from 7.62 mm dia. × 57 mm long, as-fused, cylindrical blanks. The tests were conducted in accordance with ASTM E8-Standard Test Methods for Tension Testing of Metallic Materials [32]. The elastic strain rate was approximately $3 \times 10^{-5}\ s^{-1}$ and the actuator displacement rate was maintained at a constant speed throughout the test. The elongation at fracture was taken as the strain corresponding to a 10% load drop from the maximum load.

Fracture surfaces of failed tensile samples were imaged using an SEM with SE detector. Representative samples were selected based on tensile test behavior, avoiding those samples that failed outside the gage section or had outlier properties.

## 3. Results

### 3.1. Powder characterization

Table 2 provides the measured powder composition determined via XRF. There were no major changes in composition upon powder treatment. It was noted for both normal and treated powders that the Cr content is slightly above specification, while the S content is considerably higher than the specification limit. Fig. 4 shows particle size and sphericity measured by optical statistics. Fig. 4a shows the particle size distribution. In general, the treated powder size distribution was skewed towards larger diameters. The powder treatment reduced the quantity of fines, creating a skewed bimodal size distribution with an increased average mean size. Fig. 4b shows the same results with particles binned by volume percent of particles below the specified diameter. In this case, the treated powder was larger for each size class. The sphericity, which is the ratio of the circle area to the circumference squared, is shown in Fig. 4c. There is no statistical change in sphericity in the 10% and 50% bins and a slight increase in the largest size bin for treated powder. The aspect ratio (Fig. 4d) is the smallest of all the maximum chords of the particle projection divided by the greatest distance between two pixels on the circumference of the particle projection. The aspect ratio was slightly higher for treated versus normal across all size bins.

In contrast, Fig. 5 shows SEM micrographs of the two powder lots which qualitatively indicate treated powder (Fig. 5c) appears rounder and more uniform than the normal particle (Fig. 5a). Fig. 5d, the treated particle surface, clearly shows the formation of satellites post treatment compared to the normal particle (Fig. 5b). The satellites are shown at a higher magnification in Fig. 5e with a comparison of the composition of the satellites relative to "planet" particle measured by EDS (Fig. 5f). The satellites were depleted in Fe and Ni and enriched in Cr and Mn. The amount of Mo remained similar.

Crystalline phases present in the powder samples were characterized with XRD. The normal SS 316L powder exhibited a diffraction pattern shown in Fig. 6. Over the range of angles assessed, five discrete peaks were associated with the FCC γ-austenite phase expected for this class of stainless steel. The treated powder, however, exhibited a second phase in addition to the austenite. Fig. 6 shows three peaks associated with BCC ferrite, likely a retained δ phase (peaks were indexed from an α phase ferrite reference, but the crystal structure, BCC Im-3m, is the same for both). In addition, there is an indication that the austenite peaks become narrower as a result of the treatment process, as assessed by the full width at half maximum (FWHM) parameter (for planes (111) and (200), for example).

The presence of ferrite in the treated powder was cross-validated with VSM, as δ-ferrite (a ferromagnetic material) has markedly different magnetic behavior than γ-austenite (a paramagnetic material). Fig. 7a shows the stark difference in powder response to the externally applied magnetic field. The treated powder is much more sensitive to the field than the normal powder and has a higher magnetic moment throughout. The paramagnetic contribution from the austenite phase was calculated from the linear response each powder exhibited in the high field regime. By removing this contribution, the ferromagnetic contribution of the ferrite phase was isolated. Fig. 7b shows the isolated contributions for the normal powder and reveals that the saturation magnetization is 0.93 emu/g. Conversely, the treated powder exhibited a saturation magnetization of 7.7 emu/g. Following the procedure utilized by Pinto et al. [21], but using the corrected saturation magnetization value for ferrite (218 emu/g) taken from Crangle and Goodman [33] instead of that for martensite, which Pinto et al. cited from Mumtaz et al. as 154 emu/g [34], the volume fraction of ferrite can be approximated. The normal powder contained approximately 0.43 vol percent ferrite and the treated powder contained approximately 3.5 vol percent

**Table 2**
Powder composition determined via XRF. All values in wt %. The percent difference between the two powder compositions is calculated.

| Wt % | Fe | Cr | Ni | Mo | Mn | Si | S | C | Cr Eq. | Ni Eq. [DeLong] |
|---|---|---|---|---|---|---|---|---|---|---|
| Specification | Balance | 16–18 | 10–14 | 2–3 | <2 | <1 | <0.03 | <0.03 | ~21 | ~14 |
| Normal | 62.14 | 20.08 | 11.7 | 3.8 | 1.66 | – | 0.44 | – | ~24 | ~13 |
| Treated | 63.21 | 19.03 | 12.19 | 3.75 | 1.18 | 0.15 | 0.49 | – | ~23 | ~13 |
| Percent Difference | 1.07 | −1.05 | 0.49 | −0.05 | −0.48 | 0.15 | 0.05 | – | ~-1 | ~0 |

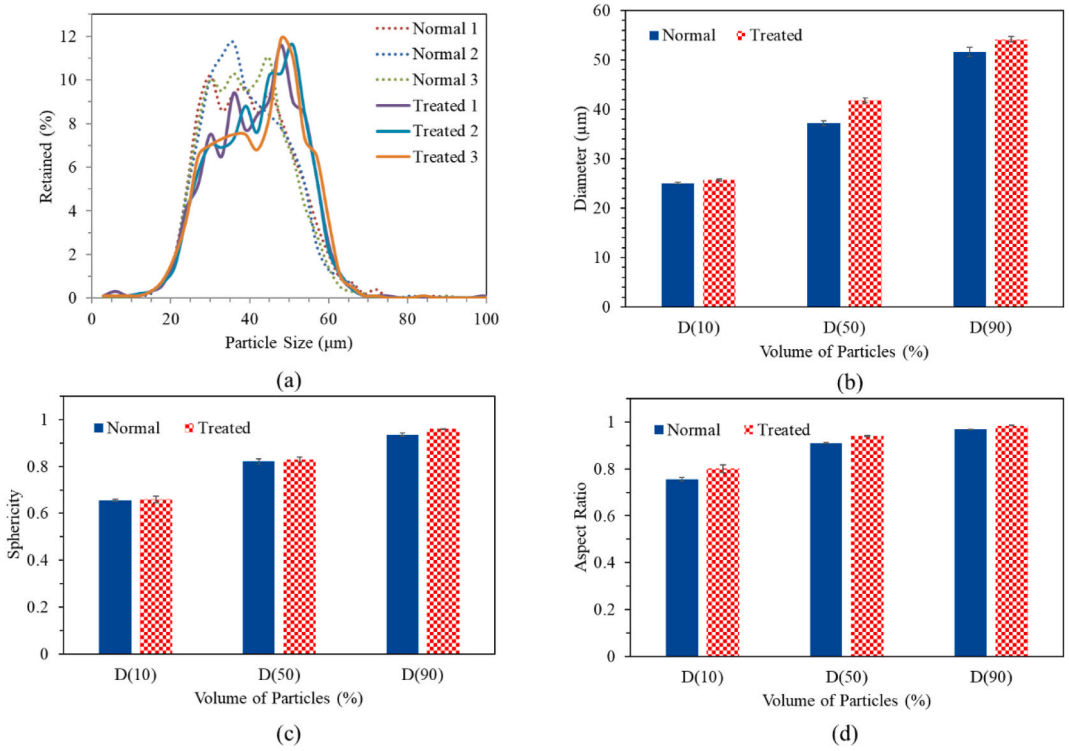


**Fig. 4.** a) Particle size, b) particle diameter c) sphericity and d) aspect ratio measured by optical statistics using a Camsizer X2® instrumentation.

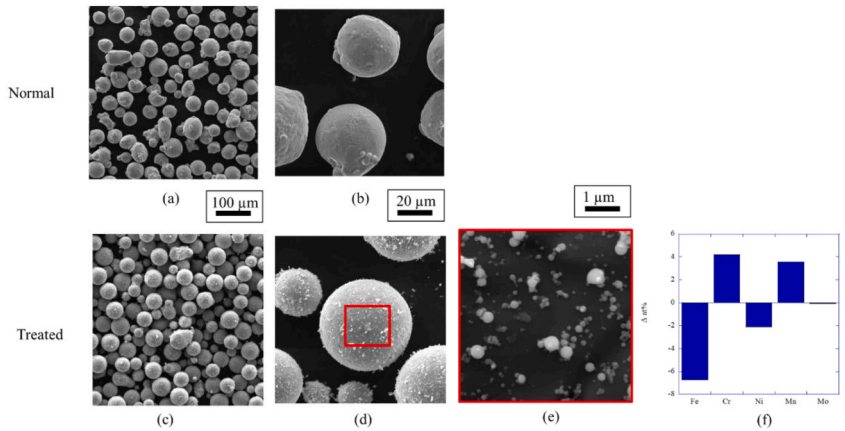


**Fig. 5.** SEM SE micrographs of a)-b) normal and c)-e) treated powder mounted on sample prior to build process. e) Satellite formation on the treated particles. F) A comparison of the satellite to "planet" particle change in atomic % measured by EDS as exemplified in e).

ferrite, calculated from Fig. 7c. Additionally, from the hysteresis loop, it is seen that both powders initially have no intrinsic magnetic moment when the experiment begins and they both fail to retain magnetization after being exposed to the high magnetic field, as indicated by the small coercivity ($H_c$) and remanence values.

The presence of body centered cubic (BCC) ferrite was also verified using EBSD and is shown in Fig. 8. Treated powder was mounted in epoxy resin and vibratory polished to an EBSD quality finish. The majority (91%) of treated powder particles were entirely FCC (Fig. 8b). However, 7% of the particles (Fig. 8c) were BCC only and 2% were polycrystalline mixtures of FCC and BCC. Interestingly, the BCC particles were typically single crystal, whereas most (87.5%) of the FCC particles were polycrystalline. BCC phases were not detected in the normal powder via this technique. Note that the total number of particles imaged due to the difficulty of the technique was 88, with 6 BCC particles so it was not possible to determine a statistically significant values for ferrite size.

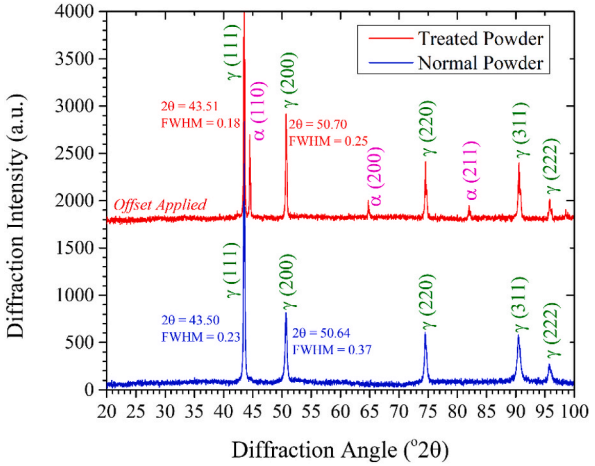


**Fig. 6.** X-ray diffractograms for normal (blue) and treated (red, offset) powder. (For interpretation of the references to colour in this figure legend, the reader is referred to the Web version of this article.)

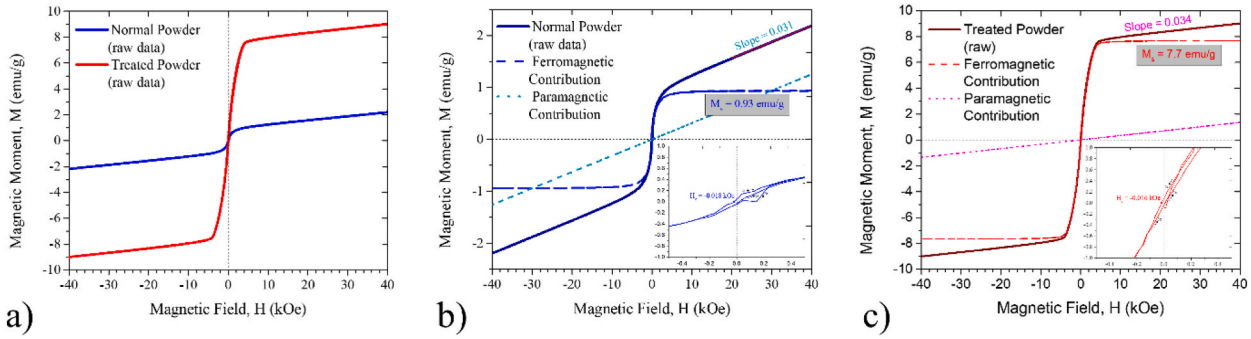


**Fig. 7.** Raw magnetic hysteresis loops of a) the normal (blue) and treated (red) powders. The isolated ferromagnetic and paramagnetic contributions of the magnetic response of the b) normal powder and the c) treated powder. An insert graph shows the remnant magnetization in the low-field regime. (For interpretation of the references to colour in this figure legend, the reader is referred to the Web version of this article.)

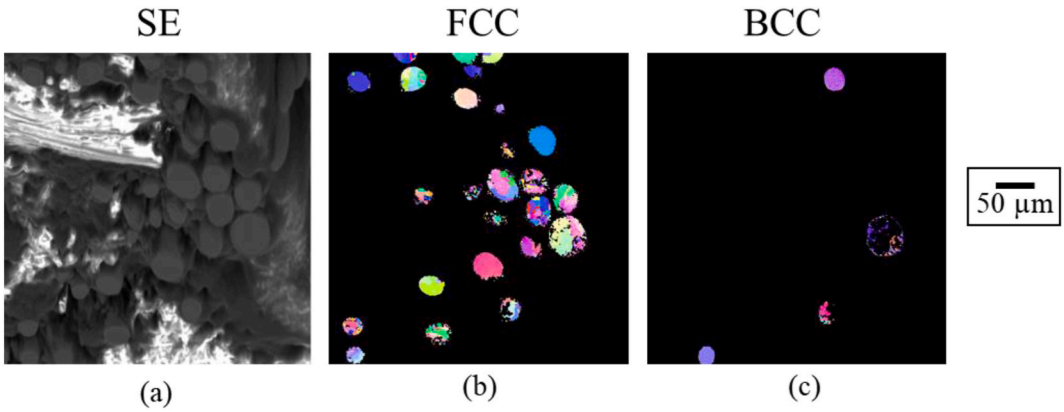


**Fig. 8.** a) SEM and b)/c) EBSD of treated powder mounted in epoxy resin. IPF from epoxy were removed to ease viewing of FCC versus BCC. Some powder was not polished due to being mounted at a lower height and thus was not visible via EBSD. (For interpretation of the references to colour in this figure legend, the reader is referred to the Web version of this article.)

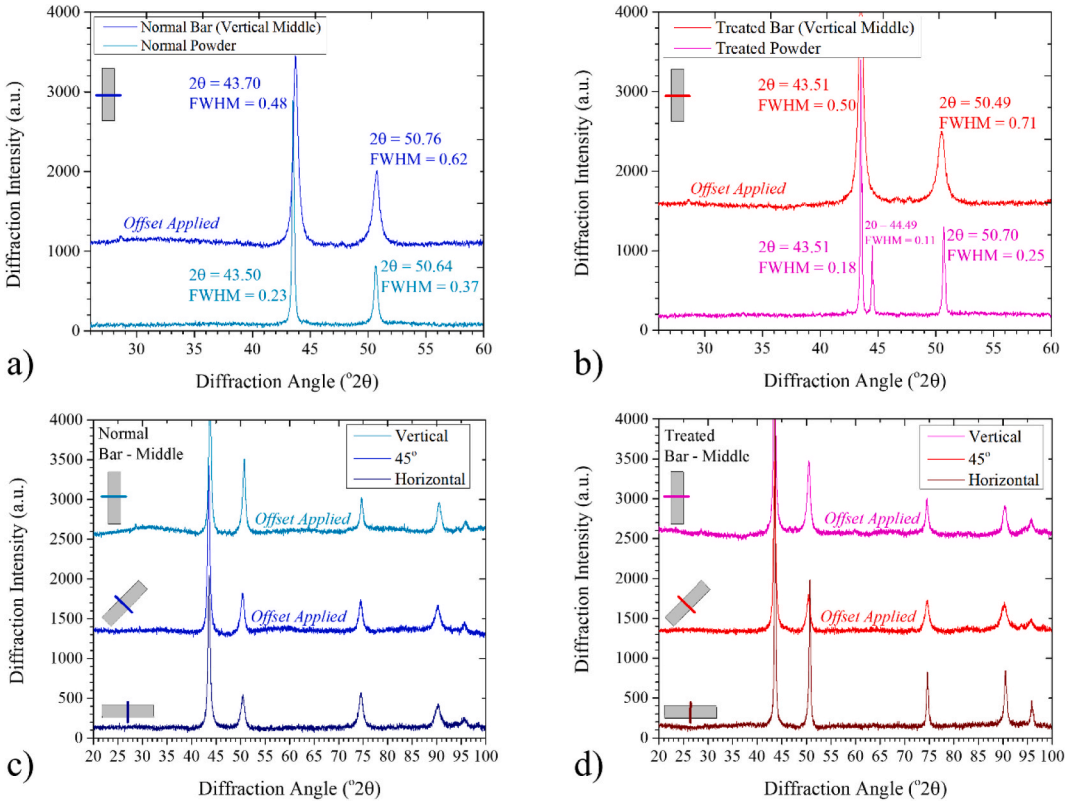


**Fig. 9.** X-ray diffractograms compared for a) normal powder versus build and b) treated powder versus build. X-ray diffractograms for the three build directions are shown for c) normal and d) treated build.

### 3.2. Build characterization

XRD was deployed to assess the crystalline phase composition of the printed bars and is shown in Fig. 9. Within the limits of detection of this technique, only the austenite phase was identified for all of the prints (Fig. 9c and d). XRD assessment suggests that there was low variability in the crystal structure as a function of build orientation. While the overall phase identity of the steel was unchanged as a function of powder type and build orientation, slight differences in peak width and height are noticeable. For example, comparing the diffraction pattern of each powder to its corresponding print in the middle of the vertically oriented bar (Fig. 9a and b) shows that there is significant peak broadening in the printed bars. The FWHM (111) for the normal powder is 0.23 while the FWHM (111) for the normal vertical print is 0.48. Likewise, the FWHM (111) for the treated powder is 0.18 while the FWHM (111) for the treated vertical print is 0.5. Peak broadening for the printed samples is attributed to residual stress in the build due to the complicated thermal history (temperature, expansion, contraction, etc.) which results from successive cycles of melting and reheating powder or build layers.

Fig. 10 shows 3 different magnification levels for the vertical build direction. Sample "slices" were taken from the middle of each build such that the surface is taken perpendicular to the long axis of the build orientation, shown in Fig. 3. Fig. 10a and b shows the normal and treated slices from the entire build; lack of fusion (LOF) type pores are observed with torturous channels and entrapped particles in areas of the sample. The treated build appears to have fewer pores. Fig. 10c,e shows two 200 μm long pores in the as built case for the normal powder. A large particle of retained powder is shown in Fig. 10d,f for the build from the treated powder. Smaller particles of retained powder are also visible within the large pores of Fig. 10c,e. Cracks are evident at sharp pore features for builds from both powder types (Fig. 10e and f). Fig. 11 shows 3 different magnification levels for the 45° build friction; similar to Fig. 10, cracks were evident coming off of sharp pore features and powder that was incompletely sintered. Visually, there was no qualitative difference in overall pore amount or size. Fig. 12 shows 3 different magnification levels for the horizontal build direction. Again, this surface is perpendicular to the long axis of the build direction (Fig. 3). It was noted that the horizontal sample was not perfectly circular (Fig. 12a and b), especially the build that used normal powder. Fig. 12c,e shows the individual build layers within a pore. Fig. 12d,f shows representative micrographs of the treated powder build, highlighting LOF defects where the individual particles are visible with unbonded interfaces between them (Fig. 12f). There are no other observable differences between the normal and treated builds.

Porosity and mean pore spherical diameter were measured with two methods. First, XCT was used to determine the volumetric porosity. Results from the XCT porosity volumetric fraction and mean equivalent spherical diameter are presented in Fig. 13a and b, respectively. Porosity was generally highest in the horizontal specimens and generally lower in the 45° and vertical specimens. In the

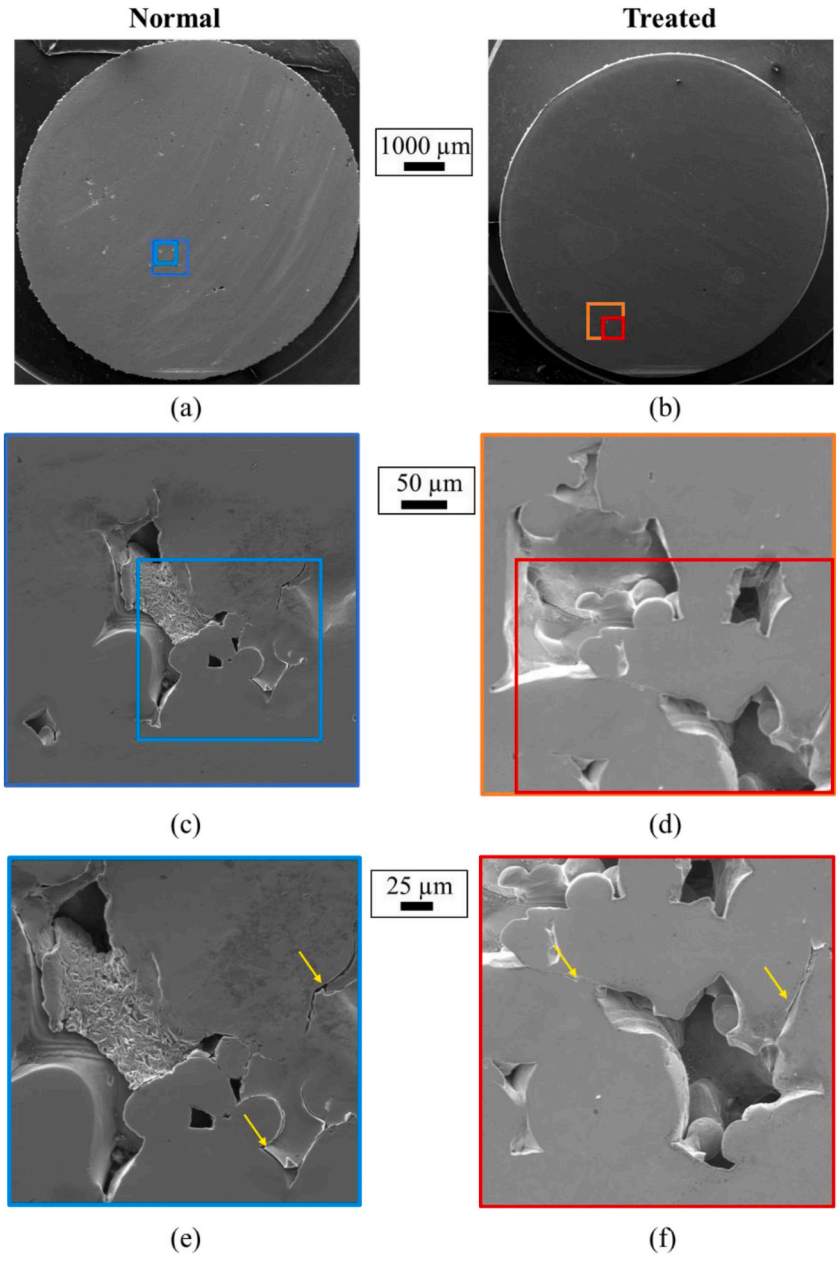


**Fig. 10.** SEM micrographs of vertical build cross section for normal and treated powder. Yellow arrows point to cracks. (For interpretation of the references to colour in this figure legend, the reader is referred to the Web version of this article.)

normal powder the 45° build direction porosity was lower than vertical but for the treated powder, it was higher. Increased porosity by definition leads to decreased theoretical density, which has been associated with loss of strength in EBM-printed Inconel 718 by Deng et al. [35]. The increase in porosity may be due to thermal conductivity. These horizontal samples enable more heat to be lost to the build plate for the earlier print layers, so the starting layer temperature is lower. This means that they have a lower starting energy and would be more likely to form a LOF pore as samples that have naturally more build heat are less likely to form a LOF pore. Additionally, the large "footprint" the horizontal samples had in the X–Y plane means that there was more time for the last printed layer to cool between printing of individual layers. The large footprint also increases the efficiency of heat transfer away from the last printed layer into the bulk of the previously printed build layers. It is also more challenging to ensure that a powder layer is spread evenly over a larger footprint of previously printed material than a small footprint layer. Inconsistent powder spreading results in defects in the build. The normal builds tended to have higher porosity than treated builds except in the case of 45° build direction. Equivalent diameter, calculated using Equation (1), was highest in the horizontal specimens and smaller in the 45° and vertical specimens. Normal builds had larger diameter pores relative to treated builds. Second, SEM was used to assess porosity in terms of area fraction. The mean

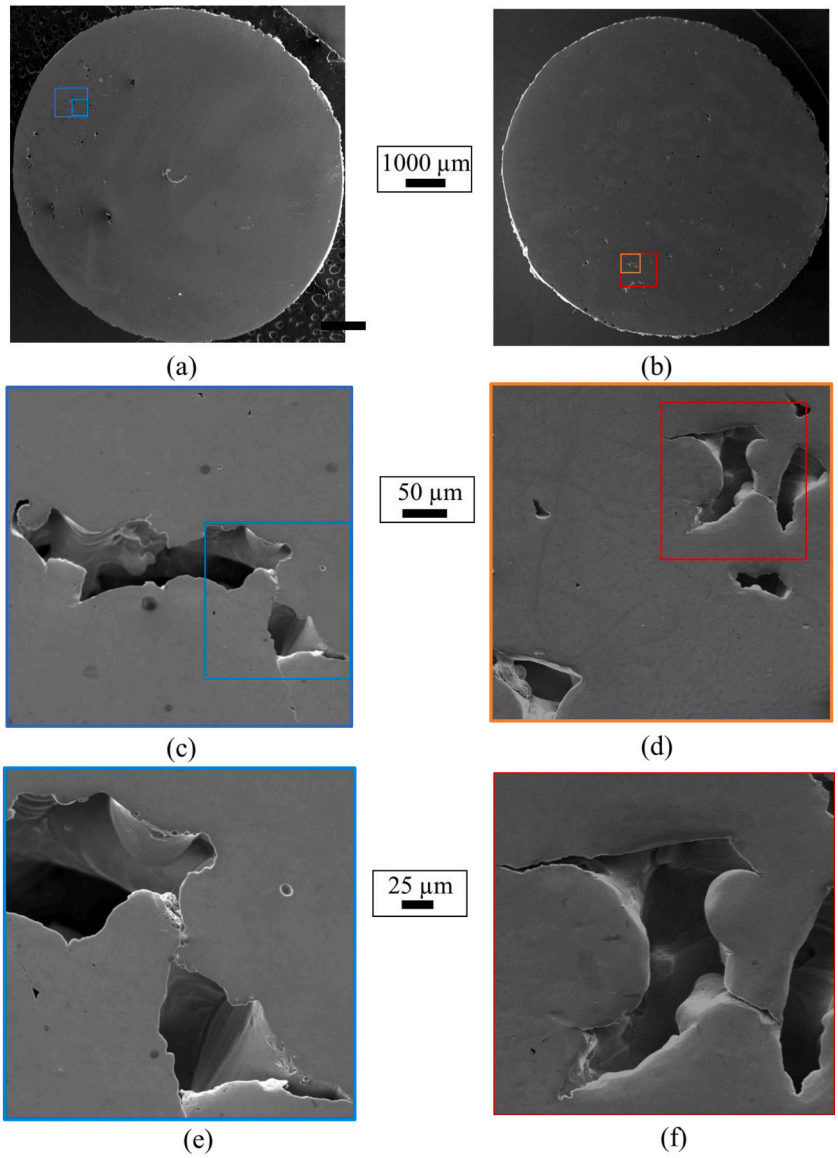


**Fig. 11.** SEM micrographs of 45° build cross section for normal and treated powder.

equivalent diameter and porosity (area fraction) from SEM are plotted in Fig. 13c and d, respectively. All trends were consistent comparing the three-dimensional XCT to the two-dimensional SEM method. Both techniques recorded porosity that was higher for the treated build than the normal build with a 45° orientation, which was not an expected result, but was nevertheless consistent with both techniques. The porosity values were the most similar: for example, the normal vertical build was measured to be 1.78 ± 0.1% and 1.46 ± 0.08%, measured by XCT and SEM, respectively. In terms of mean equivalent spherical diameter, the XCT measurements were consistently about twice as large as those measured with SEM imaging. SEM may be detecting smaller pores, accounting for this discrepancy. Nevertheless, the trends are consistent, indicating that SEM imaging can yield useful information and validate XCT porosity results.

Fig. 14 provides the grain orientation maps determined by EBSD for normal powder in the vertical (Figs. 14a), 45° (Fig. 14b) and horizontal (Fig. 14c) directions; and treated builds powder in the vertical (Figs. 14d), 45° (Fig. 14e) and horizontal (Fig. 14f) directions. Comparing the normal and treated builds, there is no observable difference in the grain structure. For vertical and 45° build directions, there appears to be a large inner grain surrounded by subgrains, obvious enough that the laser pass appears visible. The horizontal build was the most irregular with grains elongated along what appears to be the laser pass direction. The corresponding pole figures for normal and treated builds in the vertical direction (Fig. 14a,d) are presented in Fig. 15a and b, respectively. Neither normal nor treated powder exhibited a strongly preferred texture, although there was a slight decrease in the randomness from the normal to the treated build, calculated from the pole figure.

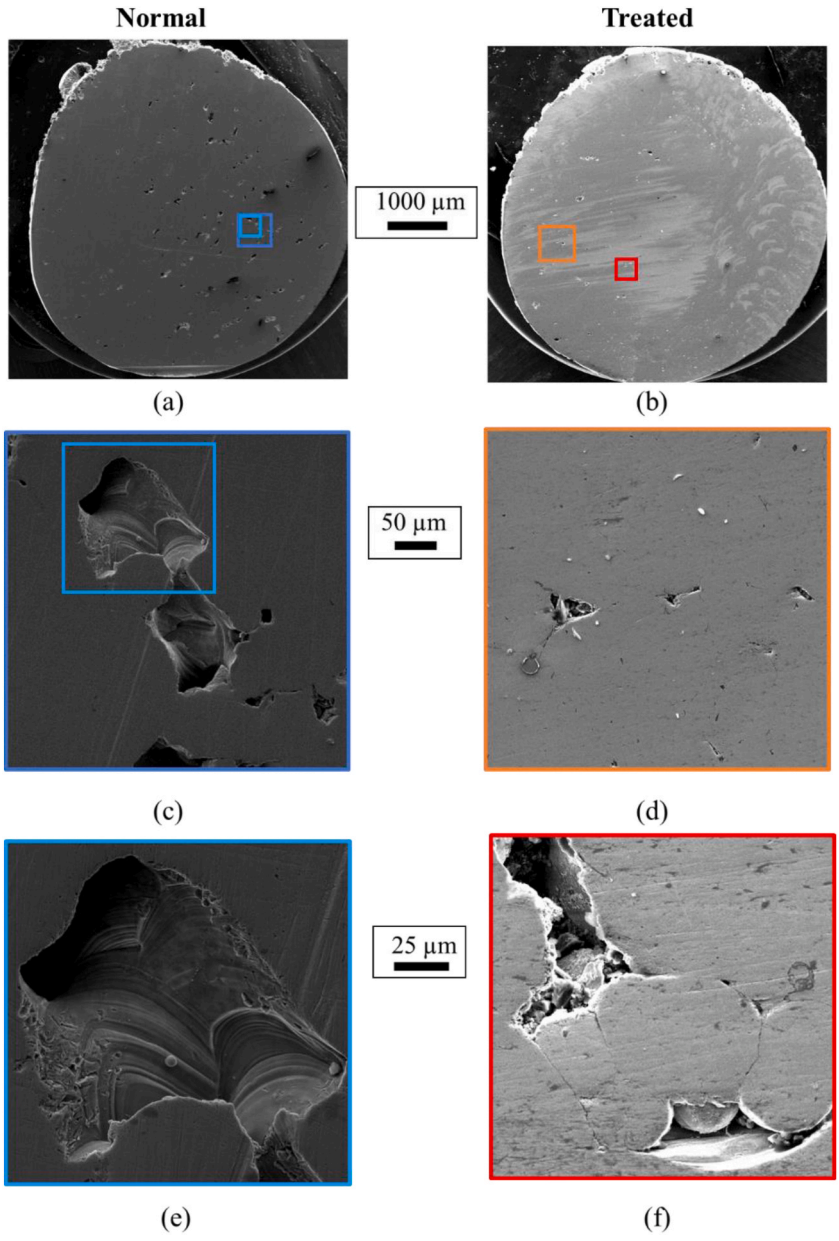


**Fig. 12.** SEM micrographs of horizontal build cross section for normal and treated powder.

### *3.3. Tensile behavior and fractography*

The mean average results of the tensile tests are presented in Table 3. The mean average yield and tensile strengths met the minimum strength requirements of ASTM F3184-16 [36]. All the individual specimens met the minimum 0.2% yield strength requirement while some of the specimens failed to meet the minimum tensile strength. The mean average elongation was generally well below the specification minimum of 30%. Of the 59 specimens tested, only 4 samples met the required elongation (these samples were made of treated powder and oriented in the vertical direction) likely due to LOF porosity, which was been characterized by XCT and SEM by Montalbano et al. in L-PBF printed Ti–6Al–4V [37]. Approximately 40% of the specimens fractured outside of the specimen gage section so elongation measurements were not available from any of those tests.

There was considerable variability in the strength properties for a given powder condition and specimen orientation. Fig. 16a and b presents box and whisker plots for the measured yield and tensile strengths, respectively. In this case, the red line represents the median average value rather than the mean average reported in Table 3. Comparing the effect of specimen orientation on the tensile behavior, the specimens oriented in the vertical direction showed the least variability while the results for the specimens in the 45° and

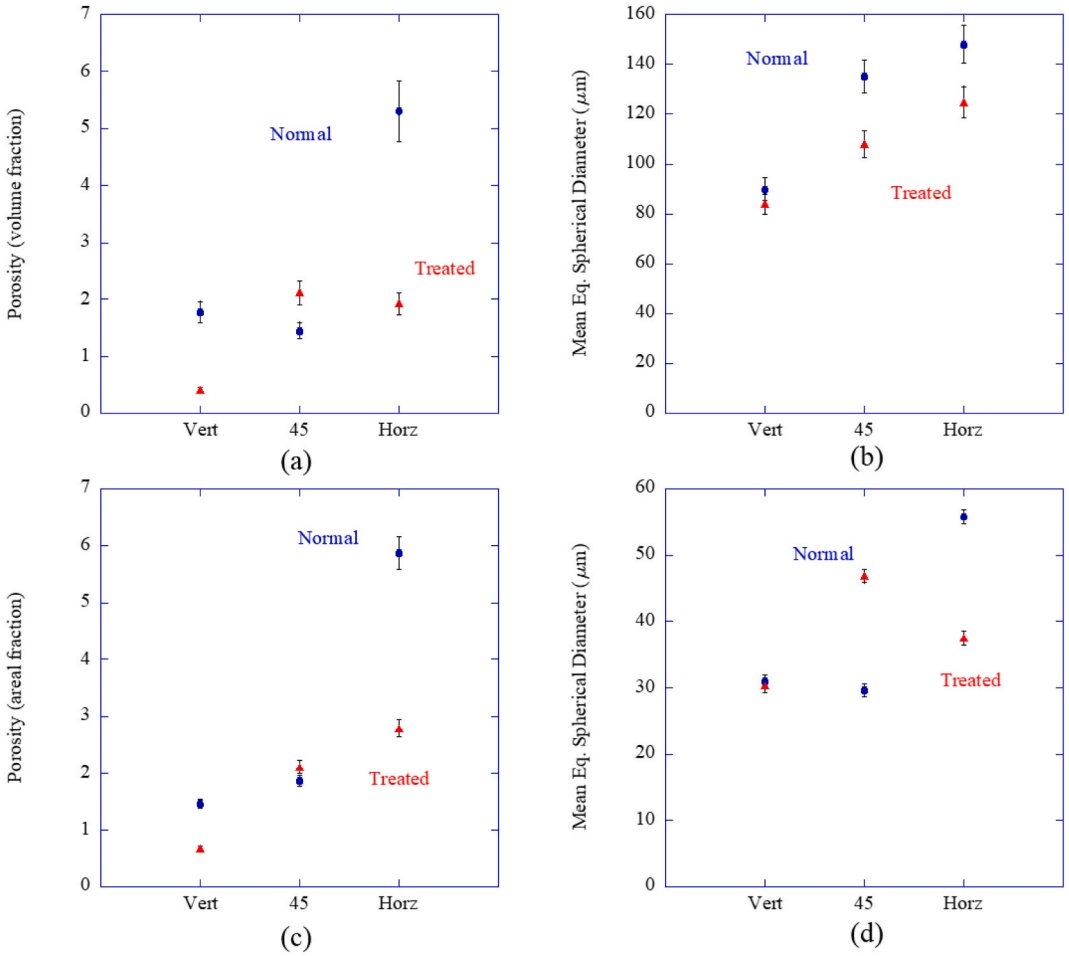


**Fig. 13.** a) Porosity (volume fraction), b) mean equivalent spherical diameter measured via XCT. c) Porosity (areal fraction) and d) mean equivalent spherical diameter measured via SEM.

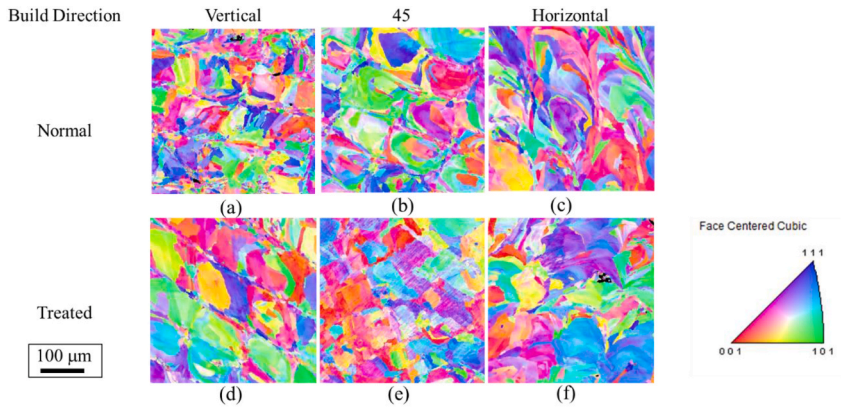


**Fig. 14.** Inverse pole figures determined by EBSD for normal and treated powder in all build directions. EBSD scans taken perpendicular to the long axis of the build orientation, consistent with Figs. 10 and 12. (For interpretation of the references to colour in this figure legend, the reader is referred to the Web version of this article.)

horizontal directions had considerably greater scatter. There was also a general trend observed as a function of powder condition with the results for the treated powder showing less variability than for the normal powder. In addition, the mean average yield strength of the specimens fabricated using the normal powder was about 6% higher than for the case of the treated powder.

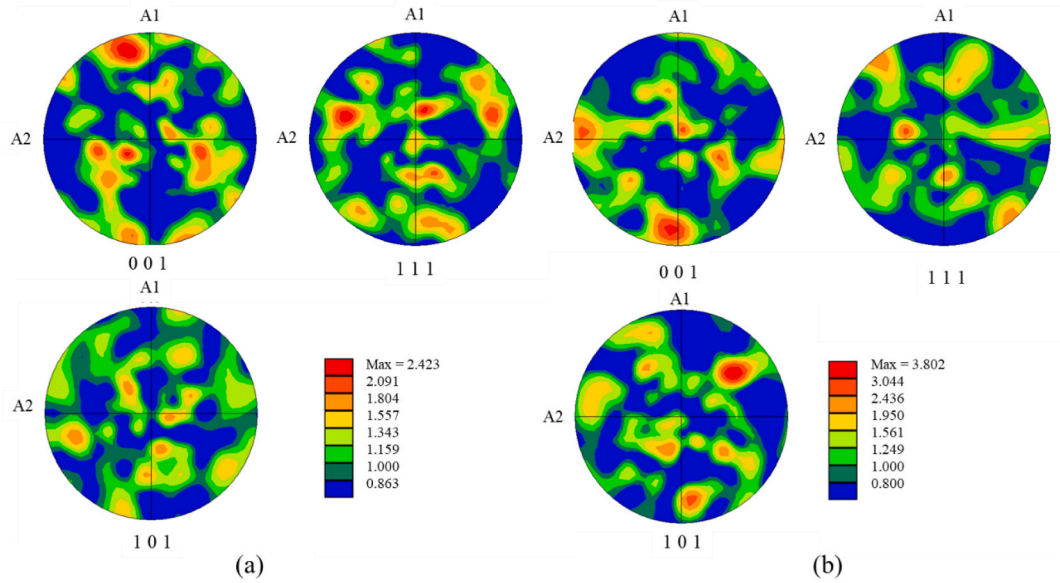


**Fig. 15.** Pole figures for a) normal and b) treated vertical builds. EBSD scans taken perpendicular to the long axis of the build orientation, as in Fig. 14. (For interpretation of the references to colour in this figure legend, the reader is referred to the Web version of this article.)

**Table 3**
Summary of mean average tensile results from specimens fabricated from normal and treated SS 316L powder stock.

| Powder Stock | Orientation | 0.2% Yield Strength MPa (ksi) | Ultimate Tensile Strength MPa (ksi) | % elongation |
|---|---|---|---|---|
| Normal SS 316L | Vertical | 495 (71.8) | 573 (83.1) | 12.0 |
| Treated SS 316L | Vertical | 455 (66.0) | 552 (80.1) | 27.8 |
| Normal SS 316L | 45° | 476 (69.0) | 530 (76.9) | 4.4 |
| Treated SS 316L | 45° | 459 (66.5) | 541 (78.5) | 15.9 |
| Normal SS 316L | Horizontal | 475 (68.9) | 515 (74.7) | 18.3 |
| Treated SS 316L | Horizontal | 444 (64.4) | 517 (75.0) | 16.5 |
| Specification min.[a] | All | 205 (30) | 515 (75) | 30 |

[a] Specification minimum properties are from ASTM F3184-16 [36] for Condition A for comparison purposes. Condition A requires stress relieving although no post-fabrication heat treatments were applied to any of the specimens.

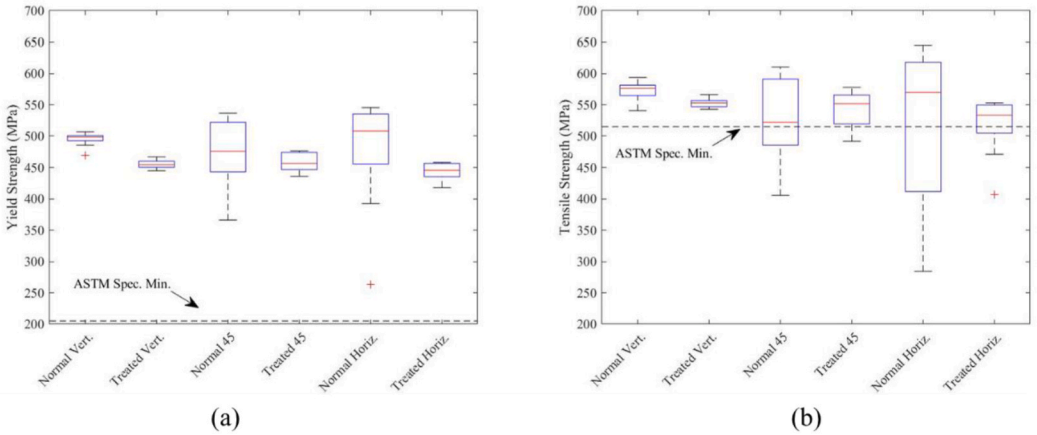


**Fig. 16.** Box and whisker plot comparison of yield and tensile strength as a function of specimen orientation and powder condition for a) normal and b) treated powder. The red line represents the median average value for each sample, the box represents the middle 50% of the observations and the whiskers show the maximum and minimum observations. The red cross represents an outlier. (For interpretation of the references to colour in this figure legend, the reader is referred to the Web version of this article.)

The median and mean average yield strength and ultimate tensile strength trends were not necessarily consistent. For the normal builds, the average yield strength in the vertical build direction, was the highest followed by 45° then horizontal, respectively. However, the median yield strength in the horizontal direction was higher than the other directions. This is a result of the large scatter in the horizontal, and to a lesser extent, the 45° build. A similar trend was observed in the treated powder with the mean average yield strength approximately the same for vertical and 45° but smaller for horizontal (444 MPa). In this case, the median yield strength tracked with average yield strength. The same trends continued with UTS except the normal, horizontal median UTS was higher than the vertical and 45° directions.

Representative fracture surfaces are shown for the normal powder condition in the vertical (Fig. 17a), 45° (Fig. 17b) and horizontal directions (Fig. 17c) and for the treated powder condition in the vertical (Figs. 17d), 45° (Fig. 17e) and horizontal directions (Fig. 17f) from each of the powder conditions and build orientations are shown in Fig. 17. While not easily observed in the top-down views, all fracture surfaces had significant roughness, on the order of ~1 mm in height variations. All fracture surfaces showed evidence of dimples and microvoids, suggesting plastic deformation. Pores containing retained powder particles were also observed. These pores were quite large, on the order of ~100 μm and often located at or near the specimen edge. All fracture surfaces, regardless of powder condition or build orientation, contained these large pores. Examples for both the normal and treated powder conditions are shown in Fig. 18a and b, respectively. Some voids are on the order of 10 μm in diameter while very small microvoids were also observed at higher magnifications (Fig. 19c).

For some specimens, voids presented in a grid-like pattern across the entire fracture surface. One such example is shown in Fig. 19a. This pattern was clearly identified on the treated specimens in the vertical orientation and normal specimens in the 45° orientation. The rest of the powder conditions and build orientations had similarly sized voids but the grid pattern over larger regions were either hard to identify (Fig. 17c) or non-existent (Fig. 17e). Multiple micrographs were selected across specimens with the same powder condition and build orientation to obtain the diameter and spacing of these void grids. Void diameter was estimated using a 3-point circular fit and void spacing was measured from center point to center point. Spacing measurements were separated as nearest neighbors in two roughly orthogonal directions, due to the grid-like pattern. Care was taken to make measurements on flat sections of the fracture surfaces to avoid any errors due to surface topography. An example micrograph is shown in Fig. 19b. For treated specimens in the vertical orientation the voids have a mean average diameter of 39 μm and void spacing of 63 μm for both orthogonal directions of nearest neighbors. For normal specimens in the 45° orientation the voids have a mean average diameter of 52 μm and void spacing of 70 μm in one direction and 76 μm in the other.

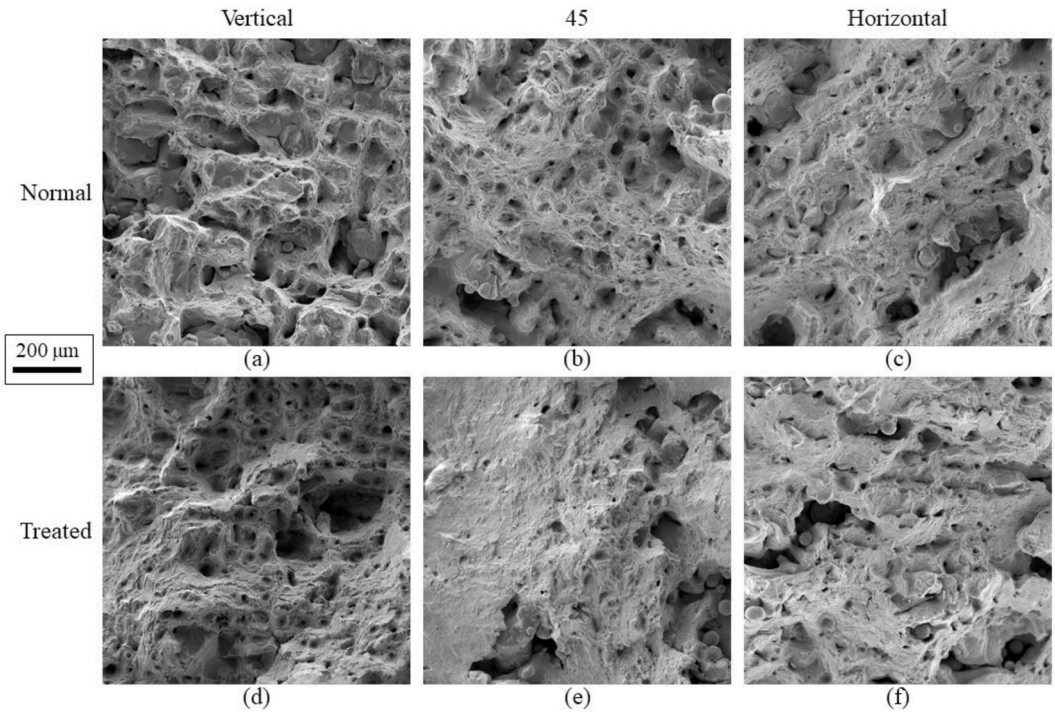


**Fig. 17.** Representative fracture surfaces from all powder conditions and specimen orientations.

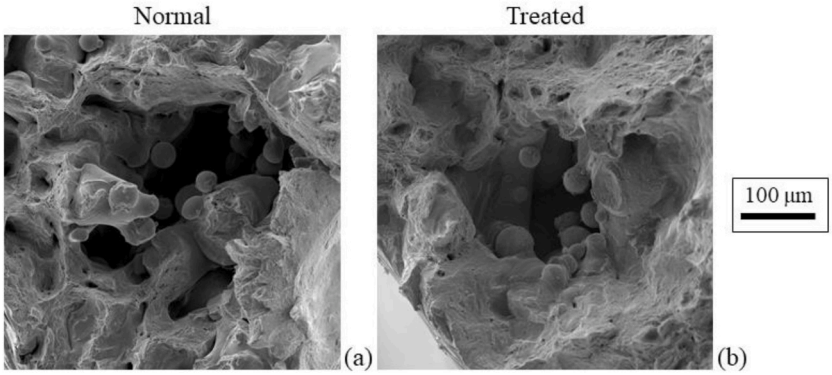


**Fig. 18.** Large pores found on fracture surfaces of a) normal powder and b) treated powder, vertical specimens near the specimen edge.

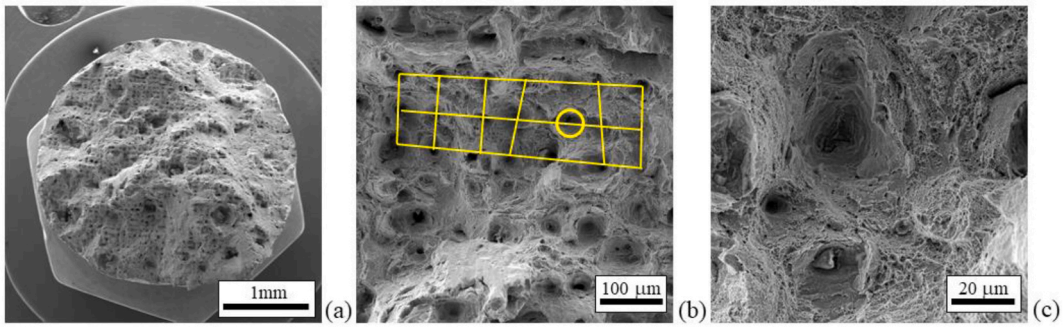


**Fig. 19.** Grid pattern of voids present in the treated powder, vertical orientation fracture surface a) at low magnification, b) with an example of nearest neighbor orthogonal directions and 3-point circle fit, and c) at high magnification.

## 4. Discussion

### *4.1. Formation and effect of ferrite*

The first noticeable effect of the plasma treatment was the introduction of ferrite as a microstructural feature. The development of ferrite in the SS 316L powder as a result of RF plasma treatment was also reported by Ji et al. [24]. More commonly, ferrite accumulation has been observed as a result of powder recycling/reuse in L-PBF [20,21]. The presence of ferrite was cross-validated with XRD (Fig. 6), magnetometry (Fig. 7), and EBSD (Fig. 8). Rietveld refinement of the powder diffraction data was executed with GSAS-II open software package [38] to arrive at an estimated ferrite weight percentage of ~15%. Magnetometry assessment of the magnetization saturation, $M_s$, of the two powder samples relative to the $M_s$ of pure iron ferrite yielded an estimated 3.5% volume fraction of ferrite in the treated powder (and 0.43% in the normal powder). The volume fraction was estimated from the EBSD analysis assuming a uniform distribution of ferrite across all particle sizes (unverified in this work) and that the small sample size observed in the EBSD map shown in Fig. 8 is representative of the entire powder population (unknown). Approximately 8% of the particles identified using EBSD were BCC ferrite and another 8% contained at least some detectable amount of ferrite along with austenite. In this way, a lower bound ferrite estimate from EBSD can be made for at least 8% by volume.

The plasma treatment takes a relatively ferrite-free material and introduces a notable amount of ferrite. Austenitic SS 316L contains enough ferrite stabilizing elements that formation of ferrite is certainly possible, as assessed with a Schaeffler diagram developed by Long and DeLong [39]. In fact, Long and DeLong quantified the volume percent of residual delta ferrite contained in welds of austenitic steels via magnetism-derived experimental measurements [39]. Using Long and DeLong's expression for equivalent chromium and nickel, SS 316L is predicted to contain 7.6% ferrite (by volume) because of heat treatment conditions associated with welding processes. This prediction falls within the range of estimates derived here from the three techniques. The 3.5% ferrite content magnetometry estimate measured here is less than the 7.6% prediction derived from Long and DeLong's magnetism assessment. However, this assessment was for welded austenitic steel. The temperature-time-transformation kinetics of the plasma treatment as well as L-PBF are likely markedly different than conventional welding techniques. Indeed, the cooling rate of SS 316L will largely determine what the final content of ferrite is, with slower cooling rate generally favoring more ferrite formation [40].

As mentioned, the high cooling rates associated with L-PBF gives rise to relatively ferrite-free microstructures, as is evidenced by the lack of corresponding BCC diffraction peaks in the XRD and EBSD data for the build specimens. The cooling rate of the plasma treatment is likely similar (but not identical) to that of welding. The EBSD map (Fig. 8) of treated powder shows a mixture of oligo-

crystalline and mono-crystalline powder particles. The mono-crystalline particles are indicative of slowly cooled liquid droplets that yielded slow crystal nucleation rate, allowing the grain to grow without competition into a larger mono-crystal. Mono-crystals are observed for both the FCC (austenite) and BCC (ferrite) crystal structure, indicating that the slower cooling rate did not necessarily favor ferrite over austenite, but every BCC-only particle was mono-crystalline. In addition to discrepancies due to differences in the cooling rate, magnetometry assessment of the powder ferrite content may also be different from Long and DeLong's prediction due to the magnetically dead zone that occurs on the outer surface of small particles [39]. This would especially underestimate the total ferrite content for small particle sizes as magnetometry is only sensitive to magnetically active ferrite. Furthermore, the ferrite content was calculated from the $M_s$ value associated with bulk ferrite, which is not necessarily the same for micro-sized ferrite.

The role of ferrite in the L-PBF printing process is not directly known. Heiden et al. and Pinto et al. both observed increasing ferrite fraction in reused powder and increasing build porosity as a function of powder recycling. The mechanism identified by Heiden et al. for increased porosity was the changing powder morphology due to powder reuse [20]. The mechanism hypothesized by Pinto et al. was the increased magnetic character of the ferrite particles resulting in particle agglomeration and poorer powder packing [21]. While not discussed by Pinto et al. this magnetism-induced agglomeration hypothesis hinges on the assumption that ferrite micro-particles behave differently than large, bulk ferrite [21]. Bulk metallic ferrite normally has a large distribution of randomly oriented domains (poly-domain, no preferential orientation) such that the net magnetic moment is zero in the absence of an applied field. In this case, two bulk ferrite samples would not attract magnetically. For a particle, as the size decreases the total number of magnetic domains per particles also decreases; such that the particle is mono-domain below a critical size; around 15 nm for metallic ferrite [41]. An oligo-domain particle may still have a net, non-zero magnetic moment if the domain population is small enough such that the distribution of domain alignments is not sufficiently randomized. In this case, two oligo-domain particles might be able to attract each other.

The magnetic particles isolated by Pinto et al. were roughly three orders of magnitude larger than the mono-domain threshold size of 15 nm [21]. While the number of domains per particle as a function of metallic ferrite particle size was not measured and cannot simply be extrapolated between two known points, because of the very large difference in size, it is more likely that the magnetic particles produced from powder reuse are poly-domain rather than oligo-domain. This makes the magnetically induced agglomeration hypothesis unlikely to account for Pinto et al.'s observations [21]. Additionally, magnetometry results from here (Fig. 7) and Pinto et al. both show no initial magnetic moment, no hysteresis, or no coercivity or remanence [21]. Furthermore, in this investigation the treated powder (which contained the ferromagnetic metallic ferrite phase, ~3.5%) produced builds of a lower porosity than the normal powder (which contained much less ferrite, ~0.43%) in all but one condition (Fig. 13). If the presence of ferrite is de facto detrimental to the printing process (via the recoating process), then there should have been more porosity with the treated powder. Instead, the presence of ferrite was not detrimental under these conditions.

The size difference between the magnetic powders observed here and in Pinto et al. is small relative to the 15 nm mono-domain threshold size [21]. For this reason, it is unlikely that size-dependent domain structure (and hence magnetic moment) accounts for the differences between the two powders. One explanation offered by Pinto et al. is that there may be a critical threshold for ferrite content above which a magnetically-induced agglomeration effect is observed [21]. It is possible that the ferrite content present within the treated powder is lower than the proposed hypothetical threshold value and the ferrite content in the recycled powder assessed by Pinto et al. was above this proposed threshold [21]. The recycled powder ferrite content was estimated by Pinto et al. at 6% by XRD Rietveld refinement, which is below the XRD estimate of 15% made here by the same XRD Rietveld refinement technique (though the data were independently collected and fitted by different researchers [21]. Regardless, if the ferrite in the powder simply does not contain a magnetic moment, then a threshold effect where having more of these particles results in magnetic agglomeration cannot exist.

There are additional effects of decreasing particle size on powder packing. In general, agglomeration increases as particle size decreases, especially below 5 μm [42], irrespective of magnetization. Given the rather large difference in the resulting powder size distribution because of powder recycling observed by Pinto et al. it is probable that the subsequent increase in porosity near the pin support structure was a result of decreasing powder size rather than of the presence of ferrite [21]. In this investigation, the difference in powder size distribution between the ferrite-free normal powder and the ferrite-containing treated powder was less severe, lending a more meaningful assessment of the role of ferrite, which has the appearance of either decreasing build porosity or simply not detrimentally affecting build porosity. In all, the hypothesis that ferrite powder particles agglomerate due to magnetic attraction and make powder packing and spreading poorer is not supported by theory, magnetometry results from Pinto et al. [21]) and printing results shown here. However, because of the changes in the powder morphology (though less drastic here than in Pinto et al.), the role of ferrite cannot be considered in isolation by this analysis, as powder morphology is likely a more obvious controlling mechanism for the build quality.

### 4.2. *Effect of plasma treatment on powder morphology*

Similar plasma treatments have been used during initial powder fabrication as well as other post fabrication spheroidizing treatments. A similar plasma treatment was investigated by Ji et al. in which the authors observed an increase in Mo, Ni, and slight increase in Cr but a decrease in Mn [24]. Results in Table 2 for this work show an increase in Ni, but decreases in Cr, Mo, Mn. The authors also observed formation of satellites like those in Fig. 5. This was also consistent with formation of satellites via a similar process in a pilot plant gas atomizer of Al powders [43], which was explained by small particles accelerating at higher rates and velocity near the larger particles causing "welding" upon impact. A last key difference from this study and [24,43] was that the starting powder was much less spherical then the normal powder here.

Another discrepancy noted in the study from Ji et al. was a bimodal particle distribution after spheroidizing i.e. a large population of ~1 μm spheres forming whereas the normal powder was an approximately normal distribution centered on an average of 45.3 μm [24]. Sphericity was not measured quantitively (the author imaged the powder using SEM), but Ji et al. visually assessed it as 100%. Based upon their images, the normal powder used in our study was qualitatively more spherical than all their spheroidized powders except for the 30 g/min condition [24].

Using the optical sizing results, the largest change due to the powder treatment observed here is in the shift in the size distribution to larger diameters and a decrease in number of fine particles, noted in Fig. 4a. There is no statistical change in sphericity in the 10% and 50% bins and only a slight increase (2.6%) in the largest size bin in the treated powder. This was unexpected as the process was intended to be spheroidizing. The aspect ratio did increase across all size classes (Fig. 4d), consistent with an overall increase in spheroidization, though the increase was strongest at the 10th volume percentile (6.1%), as the larger powder was more likely to be already spheroidized (increase in aspect ratio of 1.7%). The overall mean average sphericity and aspect ratio were calculated to be 0.807 and 0.884 for the normal powder and the overall mean average sphericity and aspect ratio were calculated to be 0.896 and 0.852. This represents an increase in sphericity of 1.2% and aspect ratio increased by 3.4%, from normal to treated powder.

In contrast, Fig. 5 shows an SEM micrograph of the powder which qualitatively shows treated powder (Fig. 5c) appearing visually rounder and more uniform than the normal particle (Fig. 5a), which was not necessarily consistent with the optical microscope results. Using the ImageJ polygon tool and counting at least 55 particles per powder condition, the mean average sphericity was increased from 0.896 ± 0.079 to 0.925 ± 0.057. The aspect ratio (minor/major axis) increased from 0.851 ± 0.125 to 0.894 ± 0.124. These reflect a modest increase of 3.2 and 5.0%, respectively, which is about twice the increase noted on Camsizer X2®.

Overall, compared to other results from the literature, the starting point in terms of sphericity, whether measured from optical results or SEM, was higher than others in the literature. For this specific powder starting from a high sphericity, the spheroidization procedure is less effective and would likely be more suitable for a recycled or poorly formed powder although there were still modest increases in sphericity and aspect ratio indicating some success of the spheroidizing treatment. The size distribution was also impacted by the plasma spheroidization treatment.

### 4.3. Mechanical properties behavior of built samples

Porosity is commonly observed in AM metals [1,44]. Porosity can form during the build process because of trapped gas or powder lack of fusion. The latter is related to insufficient energy input, resulting in powder that is not fully melted and, consequently, that which is melted does not fully penetrate the layers below. The location of LOF pores is therefore along melt track layer interfaces. These pores are often large and irregularly shaped. LOF pores are observed in all materials in this work, regardless of powder processing, as shown in Fig. 10c and d, and they are consistently larger than their corresponding mean equivalent spherical diameter obtained through XCT (Fig. 13b). There does not appear to be interlayer porosity, which was shown to be detrimental to strength and toughness by Al-Maharma et al. [45]. Other works have shown similar porosity in as-built L-PBF SS 316L [46,47]. What is unexpected is that the porosity for both materials in this study is build orientation dependent (Fig. 13), which may have been due to track-type LOF pores which are more likely to be spatially linked. Ziolkowski et al. measured porosity in as-built L-PBF SS 316L within three specimen orientations (vertical, 45°, and horizontal) using both XCT and confocal microscopy [47]. They also found build orientation dependent porosity where porosity was minimized in the 45° orientation and maximized in the vertical direction, unlike in this current work [47]. While the authors did not offer an explanation, given that the specimens were all made in a single build it is likely due to non-uniform porosity within the specimen. In this current study, each build consisted of only a single specimen orientation, therefore porosity differences are more likely a result of either specimen orientation (i.e., horizontal builds have more porosity due to increased thermal conductivity with the plate or less uniform powder spreading over a larger footprint) or build-to-build variations, despite no change in the build parameters used. As such, it is much more likely that the specimen orientation is the controlling variable.

DebRoy et al. summarized tensile mechanical properties for L-PBF SS 316L from throughout the literature [1]. The range of reported values for yield strength (287–640 MPa), UTS (317–760 MPa), and elongation (7–42%) were all very large. This is not entirely surprising as print parameters (e.g., laser power, laser speed, etc.) are different from study to study and therefore resulting microstructure characteristics and defects will vary. What is apparent, however, is that specimens loaded in the vertical direction are stronger or as strong as horizontal specimens, which is consistent with increased porosity being inversely proportional to yield and ultimate tensile strength [45]. There was not a similarly clear orientation trend in elongation. This is consistent with the results from this study in Table 3. The tensile mechanical properties are typically associated with anisotropic microstructure due to texture and columnar grain structures oriented along the build direction.

DebRoy et al. also found that for L-PBF SS 316L, higher yield and tensile strength correlates with higher elongation [1]. DebRoy et al. suggest low strength and low elongation (below 20%) are likely a consequence of higher porosity arising from thermal conditions that build and retain more heat minimizing LOF pores [1]. Note, that by this assessment, all but the treated powder in the vertical orientation have low elongation (Table 3) and should be considered as having generally higher-than-ideal porosity, especially when considered in contrast to L-PBF printing followed by post processing, such as hot isostatic pressing [47,48]. While this strength and elongation trend is observed for the treated powder specimens, it was not observed for the normal powder, in which the horizontal build orientation had the highest porosity of the three directions, but its elongation was also the largest. This behavior is likely a result of orientation dependence related to the porosity. As Casati et al. [49] and others in the literature have shown [44,47], LOF pores have low sphericity and are oriented perpendicular to the build direction, which is consistent with the planes imaged in Figs. 10, 11 and 12. These pores are defects for which crack growth resistance is weaker when tensile loads are applied along the build direction verses within the build plane. Thus, the higher porosity materials (horizontal orientation in this study) have lower strength and elongation as

expected when compared with the lower porosity materials (vertical orientation in this study). In this instance, the more susceptible orientation of fewer pores in the normal vertical builds was more detrimental to the elongation than the larger number of pores in the less susceptible orientation in the normal horizontal build. Casati et al. observed this exact behavior for a L-PBF SS 316L material [49]. In addition, they also were able to print isotropic samples without preferred texture such that directional dependences on the mechanical behavior were influenced by something other than grain orientation [49]. They thus concluded that the anisotropic mechanical properties were caused by the LOF porosity. This may explain why, in this work, the normal powder in the horizontal orientation had the highest elongation of all three orientations. The material was shown to have no significant texture preference on the plane perpendicular to the build direction which is the load plane and thus the plane relevant for strength comparisons (Fig. 15), but higher porosity (Fig. 13a,c). This suggests that at high enough porosity, the directionally dependent effects of porosity on mechanical properties are more significant than those due to grain orientation. Furthermore, Deng et al. observed similar behavior in heat treated additive manufactured Inconel 718 even mechanical properties improved with heat treatment, but it did not change the anisotropy despite decreasing the porosity [35].

It was difficult to identify significant differences in fracture surface features across the various powder conditions and build orientations. While the large, LOF pores may have influenced the fracture mechanisms in the vertical specimens more than horizontal, nearly all the specimens had higher-than-ideal porosity. It is therefore not surprising to see LOF pores, like those shown on the polished surface in Fig. 12e, present on all fracture surfaces. The roughness of the fracture surface suggests crack propagation between susceptible LOF pores rather than typical Mode-I growth. Fracture surfaces were not studied for those specimens that failed outside the gage section; however, it is suspected that the high number of invalid tests may be a result of large LOF pores present outside of the gage section. In this instance, the location of a susceptible pore outside of the gauge resulted in failure occurring there, despite the sample design. There was no powder type or orientation correlation with frequency of invalid tests. The large voids shown in Fig. 17 were not expected, especially when presented in a regular grid pattern like that in Fig. 19. It is believed that these voids formed during failure as there is no evidence of pre-existing pores of this size and frequency (and in some cases pattern) within the as-built material (Figs. 10, 11 and 12). The voids are smaller and spaced closer than the grains identified through EBSD in Fig. 14 so it does not appear to be a result of grain pullout or void initiation at grain boundaries. The fact that they are present across the entire fracture surface and span across build layers suggests they are a build defect, possibly due to balling when volumetric energy is too low usually caused by too low laser power or too high scan rate, for instance observed by Gu and Shen although no direct evidence is available to support this theory [50]. It is interesting to note that the beam diameter and hatch spacing sizes listed in Table 1 closely match the measured void diameter and void spacing respectively, which is consistent with LOF track to track type pores.

Ultimately the differences in mechanical properties between the normal and treated powder builds are slight. The normal powder specimens were found to be 6% stronger than the treated but there is greater scatter in those yield strength results, especially in the 45° and horizontal directions, as shown in Fig. 16. More and larger pores in the normal powder specimens may be the reason for the scatter in strength. While nearly all materials are considered to have higher-than-ideal porosity, the treated powder specimens overall had less porosity and smaller mean diameter than the normal powder specimens, as shown in Fig. 13. As a practical matter, the powder treatment may not be efficacious for the reasonably spherical powder in our study as opposed to that in other studies with much poorer starting morphology. As such, porosity in L-PBF steels is highly related to the chosen build parameters [43,44] and post-build heat treatments [44,45]. It is unclear from this study, what, if any, powder effects would remain if build parameters were optimized and a post-build heat treatment was used to reduce lack of fusion porosity. As it stands, the treated powder was able to produce a print of lower porosity and more repeatable mechanical behavior than the normal powder in this non-optimized printing condition.

## 5. Conclusions

- The plasma spheroidization process was shown to be mildly successful in terms of increasing the aspect ratio and sphericity measured via a Camsizer X2® and confirmed with SEM. The overall mean average sphericity and aspect ratio were calculated to be 0.807 and 0.884 for the normal powder and the overall mean average sphericity and aspect ratio for the treated were calculated to be 0.896 and 0.852, using the Camsizer X2®. Similar analysis indicated that there was a shift in the size distribution of the powder to larger diameter after the plasma treatment. The treated powder also exhibited a bimodal distribution, whereas the normal powder had a normal distribution.
- The microstructure of the powder was assessed using XRD, magnetometry, and EBSD. The normal powder was austenitic in nature whereas the plasma spheroidization process introduced the addition of primarily single crystal ferrite. The ferrite formation was attributed to the slow cooling rates of the spheroidization process and was not observed to negatively impact the quality of the resulting build.
- Ferrite introduced in the powder by the plasma treatment was not retained in the printed samples. This was attributed to the extremely high quenching rates of the L-PBF process, which favors formation of FCC austenite.
- The porosity of the as built samples was assessed using XCT and SEM. Porosity was largest in the horizontal build and smallest in the vertical, regardless of powder treatment. In general, porosity was smaller in the treated powder, except at 45° where it was approximately the same.
- The vertical direction in both powders had the highest tensile strength. Overall, the yield strength of the normal powder was 6% larger than the treated, but there was also considerably more test scatter.
- The effect of the large lack of fusion pores was more significant than the powder type in terms of the mechanical properties behavior. This behavior showed directional dependence, having a greater affect in the vertical direction than horizontal. Porosity was not directly correlated with elongation due to anisotropy from tensile testing within and along the build plane as orientation

changed. A regular void grid pattern was also observed and the void diameter and spacing was consistent with the beam diameter and hatch spacing sizes, respectively.

## Author contribution statement

E. Getto, R.J. Santucci, R. Link, E. Retzlaff, B. Croom, T. Montalbano: Performed the experiments; Analyzed and interpreted the data; Wrote the paper.

Jr., J. Gibbs: Conceived and designed the experiments; Performed the experiments; Contributed reagents, materials, analysis tools or data; Wrote the paper.

B. Baker: Conceived and designed the experiments; Performed the experiments; Wrote the paper.

M. Koul: Conceived and designed the experiments; Wrote the paper.

S. Storck: Performed the experiments; Analyzed and interpreted the data; Contributed reagents, materials, analysis tools or data; Wrote the paper.

E. Cimpoiasu: Performed the experiments; Wrote the paper.

E. Farnan: Performed the experiments.

## Data availability statement

Data associated with this study has been deposited at https://doi.org/10.17632/hhttsr69c7.1.

## Additional information

No additional information is available for this paper.

## Declaration of competing interest

The authors declare that they have no known competing financial interests or personal relationships that could have appeared to influence the work reported in this paper.

## Acknowledgments

Funding: This work was supported by the US DoD Office of the Undersecretary of Defense Corrosion Policy and Oversight Office [Technical Corrosion Collaboration] and Naval Research Laboratory [Christine Sanders, Code 6136] for salary support and the Naval Surface Warfare Center Corona Division [Rebecca Stevens & Aaron Wiest] for providing the normal and treated powder. We thank CDR Julie Spencer (USNA) and Steven Adler (A3DM) for helpful discussions and advice.

## References

[1] T. DebRoy, H.L. Wei, J.S. Zuback, T. Mukherjee, J.W. Elmer, J.O. Milewski, A.M. Beese, A. Wilson-Heid, A. De, W. Zhang, Additive manufacturing of metallic components – process, structure and properties, Prog. Mater. Sci. 92 (2018) 112–224, https://doi.org/10.1016/j.pmatsci.2017.10.001.

[2] J.R.C. Dizon, A.H. Espera, Q. Chen, R.C. Advincula, Mechanical characterization of 3D-printed polymers, Addit. Manuf. 20 (2018) 44–67, https://doi.org/10.1016/j.addma.2017.12.002.

[3] S. Mora, N.M. Pugno, D. Misseroni, 3D printed architected lattice structures by material jetting, Mater. Today 59 (2022) 107–132.

[4] M.E. Glicksman, Principles of Solidification: an Introduction to Modern Casting and Crystal Growth Concepts, Springer Sci. Bus. Media, 2010, pp. 1–520, https://doi.org/10.1007/978-1-4419-7344-3.

[5] M.J. Matthews, G. Guss, S.A. Khairallah, A.M. Rubenchik, P.J. Depond, W.E. King, Denudation of metal powder layers in laser powder bed fusion processes, Acta Mater. 114 (2016) 33–42, https://doi.org/10.1016/j.actamat.2016.05.017.

[6] H. Ali, H. Ghadbeigi, K. Mumtaz, Effect of scanning strategies on residual stress and mechanical properties of Selective Laser Melted Ti6Al4V, Mater. Sci. Eng. A. 712 (2018) 175–187, https://doi.org/10.1016/j.msea.2017.11.103.

[7] M. Taheri Andani, R. Dehghani, M.R. Karamooz-Ravari, R. Mirzaeifar, J. Ni, A study on the effect of energy input on spatter particles creation during selective laser melting process, Addit. Manuf. 20 (2018) 33–43, https://doi.org/10.1016/j.addma.2017.12.009.

[8] R. Cunningham, C. Zhao, N. Parab, C. Kantzos, J. Pauza, K. Fezzaa, T. Sun, A.D. Rollett, Keyhole threshold and morphology in laser melting revealed by ultrahigh-speed x-ray imaging, Science 363 (2019) 849–852, https://doi.org/10.1126/science.aav4687, 80-.

[9] A.T. Sutton, C.S. Kriewall, M.C. Leu, J.W. Newkirk, Powder characterisation techniques and effects of powder characteristics on part properties in powder-bed fusion processes, Virtual Phys. Prototyp. 12 (2017) 3–29, https://doi.org/10.1080/17452759.2016.1250605.

[10] Y. Zhou, S.F. Wen, B. Song, X. Zhou, Q. Teng, Q.S. Wei, Y.S. Shi, A novel titanium alloy manufactured by selective laser melting: microstructure, high temperature oxidation resistance, Mater. Des. 89 (2016) 1199–1204, https://doi.org/10.1016/j.matdes.2015.10.092.

[11] Y. Hedberg, M. Norell, P. Linhardt, H. Bergqvist, I. Odnevall Wallinder, Influence of surface oxide characteristics and speciation on corrosion, electrochemical properties and metal release of atomized 316L stainless steel powders, Int. J. Electrochem. Sci. 7 (2012) 11655–11677.

[12] H.P. Tang, M. Qian, N. Liu, X.Z. Zhang, G.Y. Yang, J. Wang, Effect of powder reuse times on additive manufacturing of Ti-6Al-4V by selective electron beam melting, JOM 67 (2015) 555–563, https://doi.org/10.1007/s11837-015-1300-4.

[13] B. Liu, R. Wildman, C. Tuck, I. Ashcroft, R. Hague, Investigaztion the effect of particle size distribution on processing parameters optimisation in selective laser melting process, 22nd Annu. Int. Solid Free. Fabr. Symp. - An Addit. Manuf. Conf. SFF 2011 (2011) 227–238.

[14] G.P. Bierwagen, T.E. Sanders, Studies of the effects of particle size distribution on the packing efficiency of particles, Powder Technol. 10 (1974) 111–119, https://doi.org/10.1016/0032-5910(74)80036-7.

[15] A. Simchi, The role of particle size on the laser sintering of iron powder, Metall. Mater. Trans. B Process Metall. Mater. Process. Sci. 35 (2004) 937–948, https://doi.org/10.1007/s11663-004-0088-3.

[16] E.O. Olakanmi, Selective laser sintering/melting (SLS/SLM) of pure Al, Al-Mg, and Al-Si powders: effect of processing conditions and powder properties, J. Mater. Process. Technol. 213 (2013) 1387–1405, https://doi.org/10.1016/j.jmatprotec.2013.03.009.

[17] A. Strondl, O. Lyckfeldt, H. Brodin, U. Ackelid, Characterization and control of powder properties for additive manufacturing, JOM 67 (2015) 549–554, https://doi.org/10.1007/s11837-015-1304-0.

[18] W.E. King, H.D. Barth, V.M. Castillo, G.F. Gallegos, J.W. Gibbs, D.E. Hahn, C. Kamath, A.M. Rubenchik, Observation of keyhole-mode laser melting in laser powder-bed fusion additive manufacturing, J. Mater. Process. Technol. 214 (2014) 2915–2925, https://doi.org/10.1016/j.jmatprotec.2014.06.005.

[19] T.L. Starr, K. Rafi, B. Stucker, C.M. Scherzer, Controlling phase composition in selective laser melted stainless steels, solid free, Fabr. Proc. (2012) 439–446.

[20] M.J. Heiden, L.A. Deibler, J.M. Rodelas, J.R. Koepke, D.J. Tung, D.J. Saiz, B.H. Jared, Evolution of 316L stainless steel feedstock due to laser powder bed fusion process, Addit. Manuf. 25 (2019) 84–103, https://doi.org/10.1016/j.addma.2018.10.019.

[21] F.C. Pinto, I.R. Souza Filho, M.J.R. Sandim, H.R.Z. Sandim, Defects in parts manufactured by selective laser melting caused by δ-ferrite in reused 316L steel powder feedstock, Addit. Manuf. 31 (2020), 100979, https://doi.org/10.1016/j.addma.2019.100979.

[22] P.R. Taylor, S.A. Pirzada, Thermal plasma processing of materials: a review, Adv. Perform. Mater. 1 (1994) 35–50, https://doi.org/10.1007/BF00705312.

[23] N. Venkatramani, Industrial plasma torches and applications, Curr. Sci. 83 (2002) 254–262.

[24] L. Ji, C. Wang, W. Wu, C. Tan, G. Wang, X.M. Duan, Spheroidization by plasma processing and characterization of stainless steel powder for 3D printing, Metall. Mater. Trans. A Phys. Metall. Mater. Sci. 48 (2017) 4831–4841, https://doi.org/10.1007/s11661-017-4240-5.

[25] M.I. Boulos, New frontiers in thermal plasmas from space to nanomaterials, Nucl. Eng. Technol. 44 (2012) 1–8, https://doi.org/10.5516/NET.77.2012.001.

[26] J. Schindelin, I. Arganda-Carreras, E. Frise, V. Kaynig, M. Longair, T. Pietzsch, S. Preibisch, C. Rueden, S. Saalfeld, B. Schmid, J.Y. Tinevez, D.J. White, V. Hartenstein, K. Eliceiri, P. Tomancak, A. Cardona, Fiji: an open-source platform for biological-image analysis, Nat. Methods 9 (2012) 676–682, https://doi.org/10.1038/nmeth.2019.

[27] Elizabeth Getto, Raymond Santucci, Powder Plasma Spheroidization and the Characterization of SS 316L Powder and L- PBF Builds", Mendeley Data, V1, 2022, 17632 https://doi.org/10.17632/hhttsr69c7.1, 10.17632/hhttsr69c7.1, (2022).

[28] D.B. Hann, J. Iammi, J. Folkes, A simple methodology for predicting laser-weld properties from material and laser parameters, J. Phys. D Appl. Phys. 44 (2011), https://doi.org/10.1088/0022-3727/44/44/445401.

[29] M. Matthews, J. Trapp, G. Guss, A. Rubenchik, Direct measurements of laser absorptivity during metal melt pool formation associated with powder bed fusion additive manufacturing processes, J. Laser Appl. 30 (2018), 032302, https://doi.org/10.2351/1.5040636.

[30] P. Bidare, R.R.J. Maier, R.J. Beck, J.D. Shephard, A.J. Moore, An open-architecture metal powder bed fusion system for in-situ process measurements, Addit. Manuf. 16 (2017) 177–185, https://doi.org/10.1016/j.addma.2017.06.007.

[31] A. F2971-13, Standard Practice for Reporting Data for Test Specimens Prepared by Additive Manufacturing, 2021.

[32] ASTM E8-04, Standard Test Methods for Tension Testing of Metallic Materials, Annu. B. ASTM Stand., 2007, pp. 1–27, https://doi.org/10.1520/E0008.

[33] J. Crangle, G.M. Goodman, The magnetization of pure iron and nickel, Proc. Roy. Soc. A. 301 (1967) 355–361.

[34] K. Mumtaz, S. Takahashi, J. Echigoya, Y. Kamada, L.F. Zhang, H. Kikuchi, K. Ara, M. Sato, Magnetic measurements of martensitic transformation in austenitic stainless steel after room temperature rolling, J. Mater. Sci. 39 (2004) 85–97, https://doi.org/10.1023/B:JMSC.0000007731.38154.e1.

[35] D. Deng, J. Moverare, R.L. Peng, H. Söderberg, Microstructure and anisotropic mechanical properties of EBM manufactured Inconel 718 and effects of post heat treatments, Mater. Sci. Eng. A. 693 (2017) 151–163, https://doi.org/10.1016/j.msea.2017.03.085.

[36] A. F3184-16, standard specification for additive manufacturing stainless steel alloy, UNS S31603) with Powder Bed Fusion 1 (2019) 1–9, https://doi.org/10.1520/F3184, i.

[37] T. Montalbano, B.N. Briggs, J.L. Waterman, S. Nimer, C. Peitsch, J. Sopcisak, D. Trigg, S. Storck, Uncovering the coupled impact of defect morphology and microstructure on the tensile behavior of Ti-6Al-4V fabricated via laser powder bed fusion, J. Mater. Process. Technol. 294 (2021), 117113, https://doi.org/10.1016/j.jmatprotec.2021.117113.

[38] B.H. Toby, R.B. Von Dreele, GSAS-II-the Genesis of a Modern Open-Source All Purpose Crystallography Software package.Pdf, 2013, https://doi.org/10.1107/S0021889813003531.

[39] C.J. Long, W.T. DeLong, The ferrite content of austenitic stainless steel weld metal, Weld. Res. (1973) 281–297.

[40] M.A. Melia, H.D.A. Nguyen, J.M. Rodelas, E.J. Schindelholz, Corrosion properties of 304L stainless steel made by directed energy deposition additive manufacturing, Corrosion Sci. 152 (2019) 20–30, https://doi.org/10.1016/j.corsci.2019.02.029.

[41] X. Batlle, A. Labarta, Finite-size effects in fine particles: magnetic and transport properties, J. Phys. D Appl. Phys. 35 (2002), https://doi.org/10.1088/0022-3727/35/6/201.

[42] A.B. Spierings, G. Levy, Comparison of density of stainless steel 316L parts produced with selective laser melting using different powder grades, in: DL Bourell (Ed.), Proceedings of the annual international solid freeform fabrication symposium, August 2009, pp. 342–353. Austin, TX, 5.

[43] S. Özbilen, Satellite formation mechanism in gas atomized powders, Powder Metall. 42 (1999) 70–78, https://doi.org/10.1179/pom.1999.42.1.70.

[44] S.R. Narasimharaju, W. Zeng, T.L. See, Z. Zhu, P. Scott, X. Jiang, S. Lou, A comprehensive review on laser powder bed fusion of steels: processing, microstructure, defects and control methods, mechanical properties, current challenges and future trends, J. Manuf. Process. 75 (2022) 375–414, https://doi.org/10.1016/j.jmapro.2021.12.033.

[45] A.Y. Al-Maharma, S.P. Patil, B. Markert, Effects of porosity on the mechanical properties of additively manufactured components: a critical review, Mater. Res. Express 7 (2020), 122001, https://doi.org/10.1088/2053-1591/abcc5d.

[46] E. Tascioglu, Y. Karabulut, Y. Kaynak, Influence of heat treatment temperature on the microstructural, mechanical, and wear behavior of 316L stainless steel fabricated by laser powder bed additive manufacturing, Int. J. Adv. Manuf. Technol. 107 (2020) 1947–1956.

[47] G. Ziółkowski, E. Chlebus, P. Szymczyk, J. Kurzac, Application of X-ray CT method for discontinuity and porosity detection in 316L stainless steel parts produced with SLM technology, Arch. Civ. Mech. Eng. 14 (2014) 608–614, https://doi.org/10.1016/j.acme.2014.02.003.

[48] S. Gangireddy, E.J. Faierson, R.S. Mishra, Influences of post-processing, location, orientation, and induced porosity on the dynamic compression behavior of Ti–6Al–4V alloy built through additive manufacturing, J. Dyn. Behav. Mater. 4 (2018) 441–451, https://doi.org/10.1007/s40870-018-0157-3.

[49] R. Casati, J. Lemke, M. Vedani, Microstructure and fracture behavior of 316L austenitic stainless steel produced by selective laser melting, J. Mater. Sci. Technol. 32 (2016) 738–744, https://doi.org/10.1016/J.JMST.2016.06.016.

[50] D. Gu, Y. Shen, Balling phenomena in direct laser sintering of stainless steel powder: metallurgical mechanisms and control methods, Mater. Des. 30 (2009) 2903–2910, https://doi.org/10.1016/j.matdes.2009.01.013.